The Astronomical Journal, 134:648 – 667, 2007 August

AN ATLAS OF THE CIRCUMNUCLEAR REGIONS OF 75 SEYFERT GALAXIES IN THE NEAR-ULTRAVIOLET WITH THE *HUBBLE SPACE TELESCOPE* ADVANCED CAMERA FOR SURVEYS

Víctor M. Muñoz Marín,[1] Rosa M. González Delgado,[1] Henrique R. Schmitt,[2] Roberto Cid Fernandes,[3] Enrique Pérez,[1] Thaisa Storchi-Bergmann,[4] Tim Heckman,[5] and Claus Leitherer[6]

Received 2007 February 6; accepted 2007 April 25

ABSTRACT

We present an atlas of the central regions of 75 Seyfert galaxies imaged in the near-UV with the Advanced Camera for Surveys of the *Hubble Space Telescope* at an average resolution of ∼10 pc. These data complement archival high-resolution data from the *Hubble Space Telescope* at optical and near-IR wavelengths, creating an extremely valuable data set for astronomers with a broad range of scientific interests. Our goal is to investigate the nature of the near-UV light in these objects, its relation to the circumnuclear starburst phenomenon, and the connection of this to the evolution and growth of the galaxy bulge and central black hole. In this paper we describe the near-UV morphology of the objects and characterize the near-UV emission. We estimate the size and the luminosity of the emitting regions and extract the luminosity profile. We also determine the presence of unresolved compact nuclei. In addition, the circumnuclear stellar cluster population is identified, and the contribution of the stellar clusters to the total light, at this wavelength, is estimated. The size of the sample allows us to draw robust statistical conclusions. We find that Seyfert 1 galaxies (Sy1's) are completely dominated by their bright and compact nuclei, which remains pointlike at this resolution, while we find almost no unresolved nuclei in Seyfert 2 galaxies (Sy2's). The Seyfert types 1 and 2 are quite segregated in an asymmetry versus compactness plot. Stellar clusters are found somewhat more frequently in Sy2's (in ∼70% of the galaxies) than in Sy1's (∼57%), and contribute more to the total light in Sy2's, but these two differences seem to be mostly due to the large contribution of the compact nuclei in Sy1's, as the luminosity distribution of the clusters is similar in both Seyfert types.

Key words: atlases — galaxies: nuclei — galaxies: Seyfert — galaxies: starburst — galaxies: star clusters

Online material: color figures, extended figure sets

1. INTRODUCTION

The origin of the near-UV continuum in Seyfert 2 nuclei has been a matter of debate for the last decade. In the framework of the unified model (Antonucci 1993), it was first thought that this blue continuum was scattered light from the hidden Seyfert 1 nucleus. Evidence for this picture came mainly from the discovery of broad emission lines in the polarized light of Seyfert 2 nuclei (Antonucci & Miller 1985; Miller & Goodrich 1990) and high-excitation gas extending out from the nucleus with conical or biconical morphology (e.g., Wilson et al. 1988; Tadhunter & Tsvetanov 1989; Pérez et al. 1989). However, other optical spectropolarimetry studies (Tran 1995) showed that the polarization of the continuum is lower than that of the broad emission lines, even after the subtraction of an old stellar population typical of the bulge of early-type disk galaxies. This result is well understood only if the blue continuum is dominated by another source rather than scattered AGN light. Terlevich et al. (1990) proposed a stellar origin for this continuum, and Cid Fernandes & Terlevich (1995) proposed that a heavily reddened starburst provides this emission.

The starburst origin for the blue continuum is strongly supported by *Hubble Space Telescope* (*HST*) observations. Direct observational evidence that only a small fraction of the total UV light detected in Seyfert 2 galaxies (Sy2's) is emitted by a hidden nucleus comes from high-resolution UV images of these objects (Heckman et al. 1997; Colina et al. 1997; González Delgado et al. 1998). Powerful circumnuclear starbursts have been unambiguously identified in 40% of nearby Seyfert 2 galaxies (González Delgado et al. 2001; Cid Fernandes et al. 2001, 2004). These starbursts were originally detected by means of either UV or optical spectroscopy of the central few 100 pc. Stellar wind absorption lines in the UV spectra (Heckman et al. 1997; González Delgado et al. 1998) and/or high-order Balmer lines of H and He I, and in some cases Wolf-Rayet features (González Delgado et al. 1998, 2001; Storchi-Bergmann et al. 2000), show that young and intermediate-age stellar populations are significant, if not dominant, in the nuclear region (∼100 pc) of many Seyfert 2 galaxies.

On the other hand, it is widely believed that the center of every galaxy contains a supermassive black hole (SMBH; Magorrian et al. 1998). Strong observational correlations have been observed between the black hole mass and the velocity dispersion of the host bulge (Gebhardt et al. 2000; Ferrarese & Merritt 2000), suggesting that the formation and growth of the SMBH must be closely linked to the evolution of the bulge itself. In the past, the AGN phenomenon must have coexisted with violent star formation, but to what extent this is happening today and whether there is a causal connection between them is something that needs to be better understood. Circumnuclear star clusters are very good tracers of this process. This is because the occurrence of star

[1] Instituto de Astrofísica de Andalucía (CSIC), P.O. Box 3004, 18080 Granada, Spain; manuel@iaa.es, rosa@iaa.es.
[2] Remote Sensing Division, Naval Research Laboratory, Washington, DC 20375; and Interferometrics, Inc., Herdon, VA 20171, USA; henrique.schmitt@nrl.navy.mil.
[3] Departamento de Física-CFM, Universidade Federal de Santa Catarina, C.P. 476, 88040-900 Florianópolis, SC, Brazil; cid@astro.ufsc.br.
[4] Instituto de Física, Universidade Federal do Rio Grande do Sul, C.P. 15001, 91501-970 Porto Alegre, RS, Brazil; thaisa@if.ufrgs.br.
[5] Department of Physics and Astronomy, Johns Hopkins University, Baltimore, MD 21218, USA.
[6] Space Telescope Science Institute, 3700 San Martin Drive, Baltimore, MD 21218, USA.

clusters is a common phenomenon in star-forming environments such as starburst galaxies (Meurer et al. 1995) or at the nuclei of spiral galaxies (Carollo et al. 2002; Böker et al. 2002). The nuclear star clusters, also known as stellar nuclei, have been studied spectroscopically in spiral galaxies by Walcher et al. (2006) and Rossa et al. (2006). These are massive compact star clusters whose masses seem to be correlated with the luminosities of their hosts' bulges, following the same slope as that for SMBHs. They are thus intimately linked to the evolution of the galactic bulge. Recent results support the view that SMBHs and stellar nuclei have close similarities in their formation and evolution histories (Ferrarese et al. 2006).

The determination of the properties of the nuclear and circumnuclear star cluster population is critical in order to understand the past and present evolution of the bulge and SMBH environment. High-resolution imaging combined with a high sensitivity is needed in order to resolve the nuclear star cluster population and disentangle the distribution of extended emission related to the active nucleus and the star-forming regions. In order to do that, we have performed a snapshot survey of a sample of Seyfert galaxies with the Advanced Camera for Surveys (ACS) of the *HST* in its high-resolution configuration, with the filter F330W (near-UV). This configuration is optimal for detecting faint young and middle-aged star-forming regions around these nuclei, and separating their light from the underlying bulge emission. These images complement optical and near-IR images available in the *HST* archive, providing a panchromatic atlas of the inner regions of these objects. These data will allow us to determine the frequency of circumnuclear starbursts, down to levels that cannot be observed from the ground; to characterize the properties of these clusters, such as flux, color, size, mass, and age; to study the luminosity function of star clusters and their survival rate close to the AGN; and to address questions about the relation between AGNs and starbursts, like the possible connections between the masses of black holes and luminosities of starbursts, and the implications for the evolution of the black holes and their host galaxy bulges.

In this paper we present an atlas of the observed sample. We have performed a photometric analysis, studied the presence of unresolved nuclei, and carried out a morphological analysis through structure parameters (asymmetry and compactness). We have also estimated the fraction of light coming from star clusters and compact emitting regions. In § 2 we present the sample and explain the observations and the data reduction. In § 3 we explain the analysis process and the results. In § 4 we present the conclusions of this work. We have included an appendix with a description of the main characteristics of each object.

2. CATALOG, OBSERVATIONS, AND DATA REDUCTION

2.1. *Sample Selection*

We have selected all the Seyfert galaxies in the *HST* archive that had images in these three bands: near-UV with the ACS high-resolution configuration (HRC) F330W, near-infrared with NICMOS F160W, and optical WFPC2 F606W (in most cases, but also F555W or F547M). In this paper we present an atlas of the near-UV images (*HST* ACS F330W), as well as parameters obtained from the analysis of these images. The sample is composed of the galaxies imaged as part of our proposal 9379 (PI: H. R. Schmitt), which is an *HST* Cycle 11 ACS snapshot, plus NGC 7212 and NGC 5728 from proposal 9681 (PI: S. Kraemer). These two galaxies have not been imaged with NICMOS but are included in this paper because they improve our UV study of Seyfert nuclei with their F330W images. The instrumental configuration of the observations is described in more detail in § 2.3.

The list of objects for proposal 9379 was constructed from the sample presented in Quillen et al. (2001), consisting of all the Seyfert galaxies observed with NICMOS F160W. Only objects also observed by WFPC2, most of them in F606W (Malkan et al. 1998), were included in the proposal list. From the original list of 101 objects, 73 were observed during the snapshot, making a total of 75, which allows us to carry out a statistical study for different types of Seyfert galaxies. From the final sample of 75 objects, 47 (63%) are classified as Seyfert 2 (Sy2), 14 (∼19%) as intermediate types Sy1.8–1.9, and 14 (∼19%) as Seyfert 1 and Sy1.2–1.5, hereafter referred to as Sy1.

2.2. *Sample Properties*

In Table 1 we list the basic properties of the whole sample extracted from the NED.[7] For the calculation of the distance we have used the Hubble law with $H_0 = 75$ km s^{-1} Mpc^{-1} and the radial velocity data from the NED, with the exception of objects with radial velocity $V_r \leq 1200$ km s^{-1}. For those, we used values from the literature: M81 (NGC 3031) at 3.6 Mpc (Freedman et al. 1994); Circinus at 4 Mpc (Freeman et al. 1977), and for the objects NGC 3486 (7.4 Mpc), NGC 4395 (3.6 Mpc), NGC 3982 (17 Mpc), NGC 4258 (6.8 Mpc), NGC 5005 (21.3 Mpc), NGC 5033 (18.7 Mpc), NGC 5194 (7.7 Mpc), NGC 5273 (21.3 Mpc), and NGC 6300 (14.3 Mpc) we used the values from Tully (1988).

In order to understand the possible biases of our sample we compare the general properties of our galaxies with those in two bona fide samples of Seyfert galaxies in the literature, the Center for Astrophysics (CfA) and Revised Shapley-Ames (RSA) Seyfert subsamples. From the 48 Seyfert galaxies in the CfA catalog presented in Huchra & Burg (1992; see also McLeod & Rieke 1995), 24 are in our sample as well. On the other hand, 38 out of 75 of our galaxies belong to the extended RSA Seyfert sample compiled by Maiolino & Rieke (1995) (sample D in their work). We thus explore 50% of the CfA catalog and 42% of the RSA catalog, with only 10 of our galaxies occurring in both of them. As the CfA catalog has been shown to lack some bright Seyfert galaxies, some of which are in our sample, we have used instead the extension to the CfA sample presented in Alonso-Herrero et al. (2003), in which they add a total of nine galaxies previously classified as LINERs. From now on we refer to these subsamples as CfA and RSA, respectively. The mean distance d of our sample is in between the two comparison ones, as $\langle d_{\rm RSA} \rangle =$ 34 Mpc and $\langle d_{\rm CfA} \rangle$ is 3 times larger than this (Maiolino & Rieke 1995), while the mean distance of our sample is $\langle d \rangle = 57$ Mpc. As in most of the Seyfert samples in the literature, in our sample Sy1's are, on average, more distant than Sy2's. The origin of this bias is that the luminosity of the nucleus compared to the host bulge luminosity is smaller in Sy2 than in Sy1 AGNs. Still, the distance distribution of the galaxies looks homogeneous up to 100 Mpc (Fig. 1). The standard deviation of the distribution is 41 Mpc, indicating that the range of distances is quite large. With ACS we are able to achieve a much better resolution than any ground-based study. The scale of our images ranges from less than 1 pc pixel^{-1} for the nearest objects to about 20 pc pixel^{-1} for the farthest, with a mean value of 6 pc pixel^{-1}.

We have checked for possible bias in the distribution of Hubble types among different types of Seyfert galaxies. This is plotted in Figure 2. Peculiar galaxies and those classified as uncertain are excluded. As is widely known, Seyfert nuclei are found mostly in spiral galaxies, with preference for early types (see, e.g., Moles et al. 1995 and references therein). The histograms do not seem to differ

[7] The NASA/IPAC Extragalactic Database is operated by NASA/IPAC, Caltech (http://nedwww.ipac.caltech.edu).

TABLE 1

SAMPLE PROPERTIES

Galaxy Name (1)	Alternative Name (2)	Spectral Class (3)	Hubble Type (4)	Vel. (km s^{-1}) (5)	Scale (pc arcsec^{-1}) (6)	B_T (mag) (7)	$E(B-V)$ (mag) (8)	Axial Ratio (b/a) (9)	$L_{[O\ III]}$ (10)	Ref. (11)	FIR ($10^{11}\ L_\odot$) (12)	*IRAS* F_{12}/F_{25} (13)	*IRAS* F_{25}/F_{60} (14)
CGCG 164−019		Sy2	Sa	8963	579	15.3	0.026	0.875	41.4	dG92	<0.672	0.735	0.436
Circinus	ESO 97-G13	Sy2	SA(s)b	449	19	12.1	1.455	0.435	40.21	ol94	0.135	0.275	0.275
ESO 103-G35		Sy2	SA0	3983	257	14.7	0.076	0.364	40.75	mw88	0.428	0.246	1.04
ESO 137-G34		Sy2	SAB(s)0/a?.	2747	178	12.21	0.335	0.786	41.35	fe00	<0.2597	0.392	0.325
ESO 138-G1		Sy2	E-S0	2740	177	14.7	0.2	0.5	40.12	li88	<0.186	0.273	0.664
ESO 362-G8		Sy2	Sa	4785	309	13.6	0.032	0.5	41.22	mu96	<0.156	<0.316	0.297
Fairall 49	IRAS 18325−5926	Sy2	Sa	6065	392	13.2	0.065	...	41.25	dG92	1.006	0.431	0.427
IC 2560	ESO 375-G4	Sy2	SB(r)bc	2925	189	12.53	0.095	0.625	40.51	gu06	0.2097	0.437	0.246
IC 4870	ESO 105-IG11	Sy2-HII	Pec	889	57	13.89	0.113	0.563	...[a]		<0.0073	...	<0.391
IC 5063	ESO 187-G23	Sy2	SA(s)0+	3402	220	12.89	0.061	0.667	41.28	sc03	0.6409	0.302	0.642
Mrk 6	IC 450	Sy1.5	SAB0+	5640	365	15.0	0.136	0.625	42.10	wh92	<0.3635	<0.456	0.607
Mrk 40	Arp 151	Sy1	S0-pec	6323	409	16.8	0.014	0.429	41.18	wh92	...	...	...
Mrk 42	UGC 8058	Sy1	SBb	7385	477	15.28	0.029	0.983	40.55	wh92	...	...	...
Mrk 231		Sy1	SA(rs)c?-pec	12642	817	14.41	0.010	0.769	41.91	da88	29.716	0.212	0.254
Mrk 334	UGC 6	Sy1.8-HII	Pec	6582	425	14.38	0.047	0.7	40.254	li88	<1.05	<0.238	0.246
Mrk 461	UGC 8718	Sy2	S	4856	314	14.61	0.024	0.714	40.327	cg94	...	...	...
Mrk 471	UGC 9214	Sy1.8	SBa	10263	663	14.54	0.010	0.667	40.66	da88	<0.935	...	<0.500
Mrk 477		Sy2	Compact	11310	731	15.2	0.011	0.709	43.02	wh92	<1.47	<0.463	0.4
Mrk 493	UGC 10120	Sy1	SB(r)b	9392	607	14.6	0.025	0.714	40.595	li88	<0.684	<0.926	0.422
Mrk 516		Sy1.8	Sc	8519	551	15.3	0.060	0.833	39.91	os81	<0.915	...	0.221
Mrk 915		Sy1	Sb	7228	467	14.82	0.063	0.833	42.07	wh92	<0.569	1.625	0.711
Mrk 1210	UGC 4203	Sy2	Sa;	4046	262	14.34	0.030	1.0	42.58	fa98	0.401	0.263	1.136
NGC 449	Mrk 1	Sy2	(R′)S?	4780	309	15.01	0.060	0.625	41.85	wh92	<9.727	<2.24	0.348
NGC 1144		Sy2	S-pec	8648	559	13.78	0.072	0.636	40.256	li88	2.426	0.371	0.132
NGC 1320	Mrk 607	Sy2	Sa: sp	2663	172	13.32	0.047	0.316	40.71	wh92	<0.135	0.306	0.458
NGC 1672		Sy2	(R′_1:)SB(r)bc	1331	86	10.28	0.023	0.833	38.53	gu06	0.5334	0.365	0.116
NGC 2639		Sy1.9	(R)SA(r)a:	3336	216	12.56	0.024	0.611	39.45	ho97	<0.212	...	<0.195
NGC 3031	M81	Sy1.8-L	SA(s)ab	−34	17	7.89	0.080	...	39.306	li88	0.0041	0.878	0.106
NGC 3081		Sy2	(R_1)SAB(r)0/a	2385	154	12.85	0.055	0.762	41.58	wh92	...	...	...
NGC 3227		Sy1.5	SAB(s)-pec.	1157	75	11.1	0.023	0.667	40.84	wh92	0.0755	0.385	0.218
NGC 3362		Sy2	SABc	8290	536	13.48	0.031	0.898	41.38	wh92	...	...	...
NGC 3393		Sy2	(R′)SB(s)ab	3750	242	13.09	0.075	0.909	41.98	sc03	<0.2398	<0.352	0.298
NGC 3486		Sy2	SAB(r)c	681	36	11.05	0.022	0.732	37.96	ho97	<0.0096	<1.115	0.0568
NGC 3516		Sy1.5	(R)SB(s)0	2649	171	12.5	0.042	0.765	41.35	wh92	0.1223	0.489	0.529
NGC 3786	Mrk 744	Sy1.8	(R′)SAB(r)a-pec	2678	173	13.50	0.024	0.591	40.59	wh92	...	...	...
NGC 3982		Sy2	SAB(r)b	1109	82	11.78	0.014	0.882	40.06	wh92	0.0719	0.571	0.1214
NGC 4253	Mrk 766	Sy1.5	(R′)SB(s)a:	3786	245	13.70	0.020	0.8	41.77	wh92	0.3934	0.297	0.340
NGC 4258	M106	Sy1.9-L	SAB(s)bc	448	33	9.10	0.016	0.387	41.02	ho97	...	...	...
NGC 4303	M61	Sy2-HII	SAB(rs)bc	1566	101	10.18	0.022	0.892	40.24	li88	<0.3227	...	<0.0259
NGC 4395		Sy1.8-L	SA(s)m	319	17	10.64	0.017	0.833	39.47	ho97	...	...	...
NGC 4565		Sy1.9	SA(s)b? sp	1230	80	10.42	0.015	0.116	38.71	ho97	<0.848	<1.89	0.0778
NGC 4593	Mrk 1330	Sy1	(R)SB(rs)b	2698	174	11.67	0.025	0.744	40.82	wh92	0.1637	...	<0.327
NGC 4725		Sy2	SAB(r)ab pec	1206	78	10.11	0.012	0.710	38.76	ho97	<0.214	...	<0.284
NGC 4939		Sy2	SA(s)bc	3110	201	11.9	0.041	0.509	41.847	li88	<0.183	...	<0.253
NGC 4941		Sy2	(R)SAB(r)ab:	1108	72	12.43	0.036	0.528	40.17	wh92	<0.0172	...	<0.425
NGC 5005		Sy2-L	SAB(rs)bc	946	103	10.61	0.014	0.483	39.42	ho97	0.31	0.602	0.0576

TABLE 1—*Continued*

Galaxy Name (1)	Alternative Name (2)	Spectral Class (3)	Hubble Type (4)	Vel. (km s^{-1}) (5)	Scale (pc arcsec^{-1}) (6)	B_T (mag) (7)	$E(B-V)$ (mag) (8)	Axial Ratio (b/a) (9)	$L_{[O\ III]}$ (10)	Ref. (11)	FIR ($10^{11}\ L_\odot$) (12)	*IRAS* F_{12}/F_{25} (13)	*IRAS* F_{25}/F_{60} (14)
NGC 5033		Sy1.9	SA(s)c	875	91	10.75	0.011	0.467	39.36	ho97	0.1878	0.733	0.0789
NGC 5135		Sy2	SB(l)ab	4112	266	12.88	0.060	0.692	41.28	wh92	1.599	0.270	0.153
NGC 5194	M51	Sy2-HII	SA(s)bc pec	463	37	8.96	0.035	0.616	39.14	wh92	0.0787	0.571	0.0744
NGC 5256	Mrk 266	Sy2	Pec	8353	540	14.00	0.013	...	41.08	wh92	<2.987	<0.471	0.140
NGC 5273		Sy1.9	SA(s)0	1064	103	12..4	0.010	0.893	39.48	wh92	<0.0272	...	<0.417
NGC 5283	Mrk 270	Sy2	S0?	3119	202	14.20	0.020	0.909	41.22	wh92	...	...	...
NGC 5347		Sy2	(R′)SB(rs)ab	2335	151	13.4	0.021	0.765	39.96	sc03	0.8233	0.315	0.639
NGC 5548		Sy1.5	(R′)SA(s)0/a	5149	333	13.3	0.020	0.929	41.91	wh92	0.35	0.474	0.731
NGC 5674		Sy1.9	SABc	7474	483	13.70	0.036	0.909	41.27	gu06	<0.704	...	<0.24
NGC 5695	Mrk 686	Sy2	SBb	4225	273	13.58	0.017	0.715	41.09	wh92	<0.152	...	<0.525
NGC 5728		Sy2	(R_1)SAB(r)a	2788	180	12.81	0.101	0.581	41.526	li88	<0.352	<0.395	0.096
NGC 5940		Sy1	SBab	10172	658	14.32	0.041	1.0	41.30	wh92	<0.88	...	<0.316
NGC 6300		Sy2	SB(rs)b	1109	69	10.98	0.097	0.667	39.84	sp89	0.1112	0.344	0.153
NGC 6814		Sy1.5	SAB(rs)bc	1563	101	12.06	0.183	0.933	40.26	wh92	0.0985	0.559	0.104
NGC 6951		Sy2-L	SAB(rs)bc	1424	92	11.64	0.366	0.564	38.99	ho97	0.170	0.385	0.0867
NGC 7130	IC 5135	Sy2-L	Sa pec	4842	313	12.98	0.029	0.933	41.27	sp90	2.083	0.294	0.128
NGC 7212		Sy2	Sab	7984	516	14.78	0.072	...	42.34	wh92	<1.35	<0.466	0.245
NGC 7319		Sy2	SB(s)bc pec	6747	436	14.11	0.079	0.765	41.17	wh92	...	...	...
NGC 7469		Sy1.2	(R′)SAB(rs)a	4892	316	13.0	0.069	0.733	41.84	wh92	3.599	0.237	0.203
NGC 7479		Sy2-L	SB(s)c	2381	154	11.60	0.112	0.756	38.44	dG92	0.474	0.226	0.274
NGC 7496		Sy2	(R′)SB(rs)bc	1649	107	11.91	0.010	0.909	39.60	gu06	0.134	0.178	0.178
NGC 7674	Mrk 533	Sy2-HII	SA(r)bc pec	8671	560	13.92	0.059	0.909	42.26	wh92	3.188	0.375	0.345
NGC 7743		Sy2	(R)SB(s)0+	1710	111	12.38	0.070	0.867	39.60	ho97	<0.031	...	<0.433
UGC 1214	Mrk 573	Sy2	(R)SAB(rs)0+	5174	334	13.68	0.023	1.0	42.30	wh92	<0.3358	<0.363	0.630
UGC 1395		Sy1.9	SA(rs)b	5208	337	14.18	0.075	0.769	40.89	wh92	<0.308	...	<1.8
UGC 2456	Mrk 1066	Sy2	(R)SB(s)0+	3605	233	13.64	0.132	0.588	41.20	wh92	0.763	0.216	0.221
UGC 6100		Sy2	Sa?	8844	572	14.30	0.012	0.617	41.53	sc03	<0.623	...	<0.426
UGC 12138		Sy1.8	SBa	7487	484	14.24	0.085	0.875	41.40	sc03	<0.633	...	0.477
UM 625		Sy2	S0	7492	484	17.43	0.062	0.848	41.48	Te91	...	...	...

NOTES.—Col. (1): Galaxy name. Col. (2): Alternative name. Col. (3): Spectral class: (L) LINER. Col. (4): Hubble type. Col. (5): Radial velocity. Col. (6): Angular scale calculated from the distance. Col. (7): Total asymptotic magnitude in B, B_T, from the RC3 catalog. Col. (8): Reddening $E(B-V)$. Col. (9): Axial ratio (b/a). (All these quantities but the scale were extracted from the NED.) Col. (10): Logarithm of [O III] λ5007 luminosity in units of ergs per second. Col. (11): References for col. (10). Col. (12): IR luminosity from *IRAS* fluxes calculated with the formula from Sanders & Mirabel (1996). Cols. (13), (14): *IRAS* flux ratios, F_{12}/F_{25} and F_{25}/F_{60}.

[a] IC 4870 is a Wolf-Rayet galaxy.

REFERENCES.—(cg94) Cruz-González et al. 1994; (da88) Dahari & de Robertis 1988; (dG92) de Grijp et al. 1992; (fa98) Falcke et al. 1998; (fe00) Ferruit et al. 2000; (gu06) Gu et al. 2006; (ho97) Ho et al. 1997; (li88) Lipovetsky et al. 1988; (mw88) Morris & Ward 1988; (mu96) Mulchaey et al. 1996; (ol94) Oliva et al. 1994; (os81) Osterbrock 1981; (sc03) Schmitt et al. 2003; (sp89) Storchi-Bergmann & Pastoriza 1989; (st90) Storchi-Bergmann et al. 1990; (te91) Terlevich et al. 1991; (wh92) Whittle 1992.

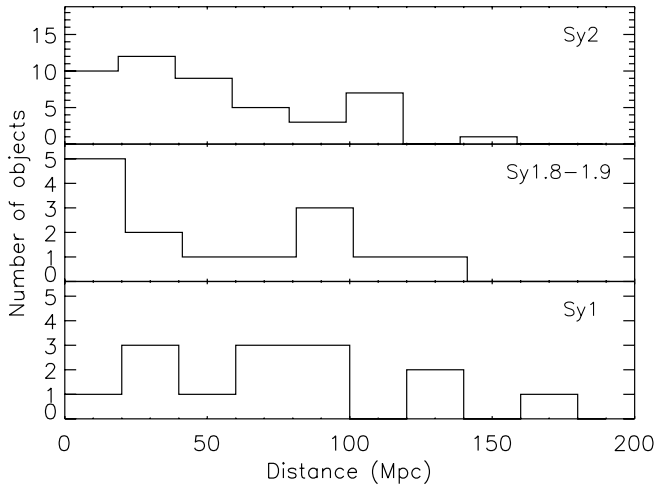

FIG. 1.—Distribution of the distances for the Sy2 (*top*), Sy1.8–1.9 (*middle*), and Sy1 galaxies (*bottom*).

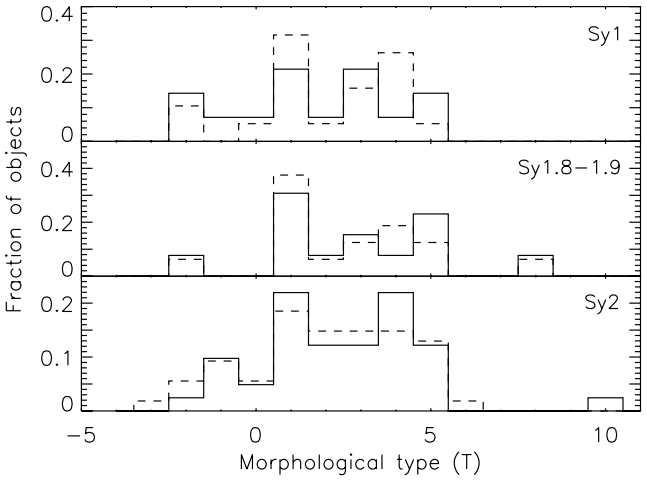

FIG. 3.—Comparison between the distribution of morphological types of our sample (*solid lines*) and the RSA sample (*dashed lines*). The histograms do not differ much. On average both samples are equivalent (see discussion in text).

much. In Figures 3 and 4 we have plotted a comparison of the CfA and RSA samples, finding a good agreement between our sample and the ones we have used for comparison. In order to quantify both statements above, we used the de Vaucouleurs classification from the RC3 catalog (T), that is, S0 $= -1$, S0a $= 0$, Sa $= 1$, Sab $= 2$, etc. The resulting mean, median, and standard deviation of the spiral types for our sample and the comparison ones are summarized in Table 2. Our three subsamples of Seyfert activity show quite similar values of mean and median T. This is enough to ensure that the differences we find among groups of activity type do not arise from differences in the Hubble morphology. Applying the same classification to the other samples we get a good matching with our own sample, although CfA galaxies tend to be of a bit earlier type.

Finally, we have obtained the distribution of the axial ratio, that is, the minor over the major axis of the galaxy (b/a). This gives an idea of the inclination angle of the galaxy, with high values for objects seen nearly face-on and low values for edge-on ones. Due to internal galactic absorption more objects with high b/a are expected, leading to a power-law distribution for a magnitude-limited sample (Maiolino & Rieke 1995). Thus, most samples, including ours, are biased against edge-on galaxies. In Figure 5 we plot the distribution of the axial ratio for the three samples. Ours is in between the less biased RSA and the CfA (more affected by this effect). This happens naturally because our sample has a mean distance in between the other two. Maiolino & Rieke (1995) find that Sy1's tend to occur more often face-on than the intermediate-type Seyfert galaxies. Within our data a slight trend in the distribution of Seyfert activity with inclination is also observed (Figure 6). This effect is not very severe, as the median value of b/a does not change much among groups, with 0.85 for Sy1, 0.75 for Sy1.8–1.9, and 0.75 for Sy2 galaxies.

2.3. *Observations and Data Reduction*

The sample was imaged with the Advanced Camera for Surveys in its high-resolution configuration (HRC), which provides a pixel size of 0.027″. The filter chosen was F330W, which, from the UV filters of ACS, has the highest throughput, negligible red leak, and minimal contamination by line emission. A higher red leak, such as that from F220W, would result in a higher background level with lower S/N detection for young star clusters. The filter F330W has a bandwidth of ∼400 Å centered around 3300 Å; therefore, the only strong emission lines contributing to this filter are [Ne v] $\lambda\lambda$3346, 3426. This type of emission is

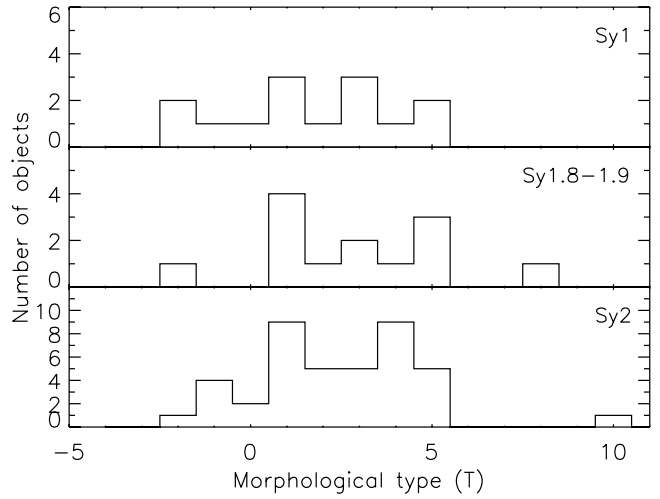

FIG. 2.—Distribution of Hubble types for the different subsamples of Seyfert activity class. The de Vaucouleurs classification (T) is used: e.g., S0 $= -1$, S0a $= 0$, Sa $= 1$, Sab $= 2$, Sb $= 3$, etc. The $T < -1$ values stand for ellipticals. The three subsamples are equivalent in average and median values.

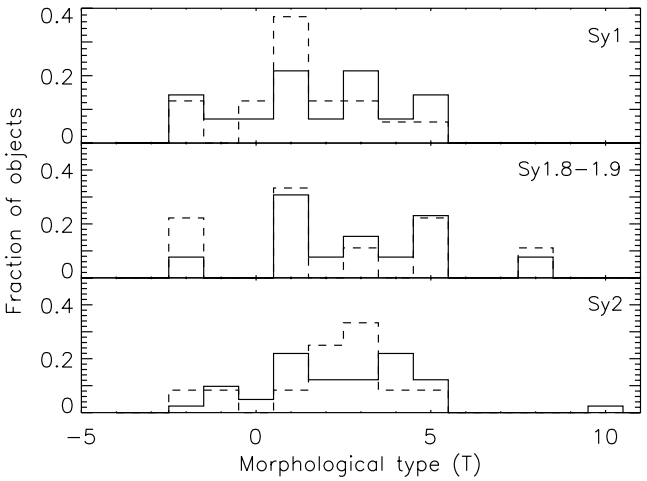

FIG. 4.—Same comparison as in Fig. 3 for our sample (*solid lines*) and CfA (*dashed lines*). These two distributions are very similar as well.

TABLE 2
STATISTICS OF HUBBLE TYPE

Type	Sample			RSA			CfA		
	Mean	Median	σ	Mean	Median	σ	Mean	Median	σ
Sy1	1.6	2	2.3	2.0	2	2.0	1.3	1	1.9
Sy1.8–1.9	2.8	3	2.6	2.8	3	2.6	2.2	1	3.3
Sy2	2.4	2	2.3	2.0	2	2.2	2.1	3	2.0

NOTES.—The table shows the mean, median and standard deviation of Hubble type for each subsample, following a de Vaucouleurs classification. All the subsamples are represented, on the mean, by early-type spirals (Sa = 1, Sab = 2, Sb = 3, etc.).

normally extended, and thus is not a problem for measuring compact objects such as clusters (see § 4).

To allow easier removal of cosmic rays (CRs), two exposures of 10 minutes each were made for a total of 1200 s. For 19 of the brightest galaxies the exposure was further split into 1140 and 60 s exposures in order to be able to study the possible saturated core. In these cases we have worked with the longest exposure when possible. The only exceptions are NGC 7212 and NGC 5728, which have 2550 s exposures.

We downloaded the images from the *HST* archive[8] with the calibration "on the fly" option, which corrects the images with bias, dark, and flat-field subtraction with the most up-to-date ACS reference files and bad pixel tables. Also, CRs are rejected, and the exposures combined into a single image. The ACS field of view is heavily distorted due to the design with a minimum number of components and a significant tilt of the detector. When projected in the sky plane, the square detector becomes rhombus-shaped. One of the automatic tasks of the ACS pipeline performs the necessary distortion correction. The final products are both astrometrically and photometrically accurate.

The pipeline CR removal task uses very mild values for the parameters, avoiding the mistaken removal of the centers of bright stars or galactic nuclei. We found that many of the images had conspicuous artifacts, such as CRs that were not removed by the pipeline. We tried out several IRAF tasks for the identification and removal of the CRs. Due to the small FWHM of the PSF (1.8 pixels) and the low S/N in some of the images, we could not get a satisfactory result with these routines. Finally, we had to remove the artifacts by hand from the regions of interest, after comparing the images with those from WFPC2 to help us to discern the CRs from small star clusters.

The background for every object was determined with the IRAF[9] task `fitsky`. The mean value and the standard deviation of the background (σ_s) was measured from several apertures in the outer regions of the image. The values of σ_s have a very low scatter (0.004–0.005 counts s^{-1}) due to the constant instrumental configuration and the similar exposure time in different images. The larger scatter of the background values (from 0.0015 to 0.005 counts s^{-1}, equivalent to 21–22.5 mag arcsec^{-2}) suggests that in some cases this is not a real sky determination but background light from the galaxy itself. As an example of this, there are some cases in which the galaxy fills the field of view (e.g., M81).

When imaging very bright objects, like some Seyfert nuclei, the possible effects of saturation have to be accounted for. The detector can reach physical saturation when more charge is released in a single pixel than what it can accumulate, resulting in charge being spilled to adjacent pixels and some flux getting lost. In particular, the default gain value of the HRC chip falls short of sampling the full well depth ($\sim$165,000 e^-) by some 22%. There are 11 objects that overcome this threshold. The core-saturated objects are Mrk 231, NGC 3227, NGC 3516, NGC 4593, NGC 5548, NGC 7469, and UGC 12138 (with a 60 s image), and Mrk 493, Mrk 915, NGC 5273, and NGC 6814 (without a 60 s image). In

[8] See http://archive.stsci.edu/hst/.

[9] IRAF (Image Reduction and Analysis Facility) is distributed by the National Optical Astronomy Observatory, which is operated by the Association of Universities for Research in Astronomy, Inc., under cooperative agreement with the National Science Foundation.

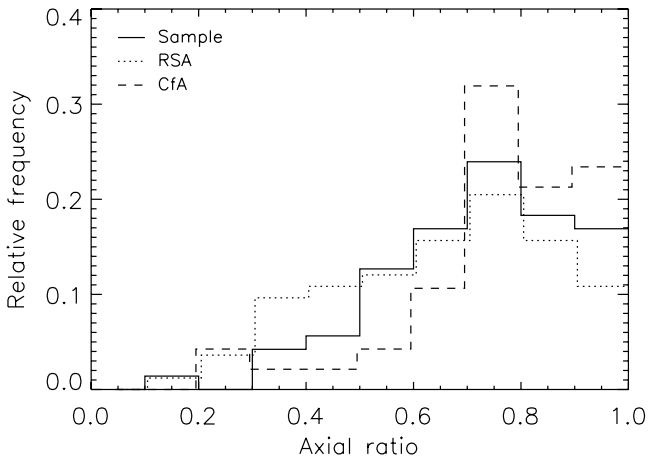

FIG. 5.—Compared histogram of the axial ratio (b/a) of the galaxies of the three different samples. Numbers are relative to the total number of objects in each sample. Our sample seems to lay in between the CfA and the RSA, and it is less biased against edge-on galaxies than the CfA.

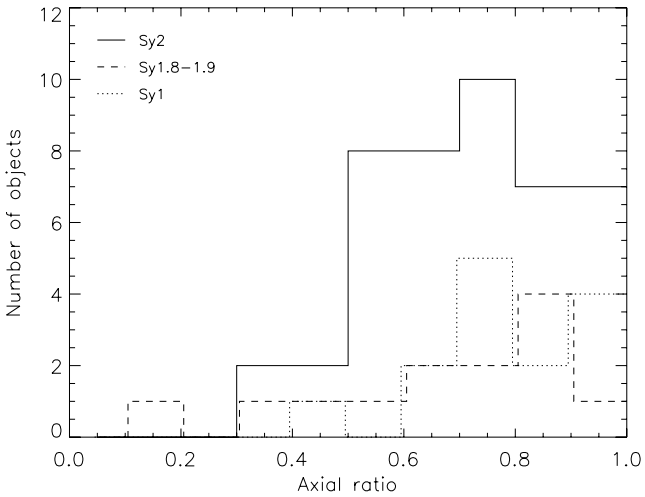

FIG. 6.—Distribution of the axial ratio (b/a) for the three activity classes. The typical trend of less objects at low inclinations is seen for this sample, although no clear trend with Seyfert type is observed. [*See the electronic edition of the Journal for a color version of this figure.*]

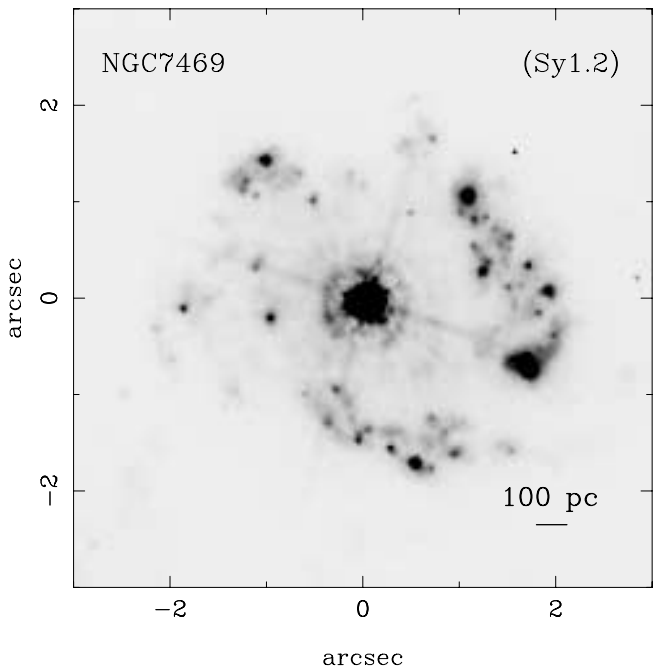

FIG. 7.14. Image of NGC 7469.

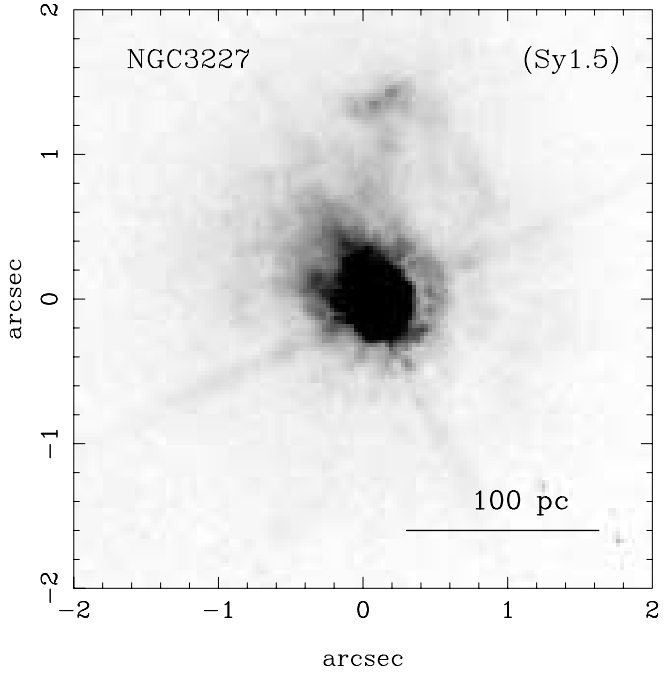

FIG. 8.1. Close-up Image of NGC 3227.

FIG. SET 7.—Near-UV ACS images. The field of view and contrast are chosen to show the most interesting parts and structure of each object. North is up, and east to the left. [*See the electronic edition of the Journal for* Figs. 7.1–7.75.]

FIG. SET 8.—Close-up images of galaxies with interesting nuclear structure or a large luminosity range within the image. [*See the electronic edition of the Journal for* Figs. 8.2–8.12.]

the cases of the objects with a 60 s image the correction to be made can be calculated by comparing the photometry between the long and short exposures. See below for further discussion.

3. RESULTS

Figure Set 7 shows the central emission of all the galaxies in the sample. We have chosen the field of view and scaling in order to enhance the most interesting features. In addition, for some galaxies we show a nuclear close-up in Figure Set 8. We have divided the objects into Seyfert types in order to better appreciate the common characteristics of each type. In the Appendix we describe the main morphological components of these galaxies, and we also show figures of all the objects showing the whole HRC field of view. The morphologies of the objects are as irregular as varied. There are many different features within the sample: star-forming rings, spirals, clumpy diffuse light emission, plain PSF-dominated objects, complete lack of a compact nucleus, etc. From Figures 7.1–7.14 it can be seen that every Sy1–1.5 galaxy possesses a bright starlike nucleus, which precludes the observation of the inner morphology. In several cases regions of star formation and rings can be seen in the images as well. The morphologies of intermediate-type Seyfert galaxies (Figs. 7.15–7.28) are more varied. Some objects have a compact nucleus. The morphology can be clumpy or diffuse, and some objects show dust absorption features or ionization cones. For the Sy2's (Figs. 7.29–7.75) the morphology is mostly clumpy, with frequent star formation regions. These are often arranged in rings or spiral arms. There are some objects showing instead a biconical or symmetrical structure, like ionization cones. When a very bright nucleus is present, as in the images of galaxies from type Sy1 to Sy1.9, some artifacts may appear, such as inner rings or clumps very close to the nucleus. These are caused by the instrumental PSF, which shows not only the diffraction spikes but also clumpy ringlike wings that can be confused with actual star-forming rings (e.g., see the image of Mrk 42, Mrk 493, or Mrk 915).

3.1. *Profiles*

Due to the irregularity of the isophotes, the common method of elliptical isophotal fitting was ruled out. Instead, we performed a photometric analysis using circular apertures. Aperture photometry was carried out with the IRAF task PHOT in order to determine the surface brightness profile and the luminosity and magnitude curves of growth. The surface brightness profile was computed by measuring the mean number of counts in circular annuli. First of all, an accurate position of the nucleus was computed when a compact source was clearly detected in the images. All the apertures were centered in the position determined by the centroid of the compact nuclear source. In the cases in which the nucleus was too obscured, an approximate position was estimated by taking as a reference the nuclear position in the WFPC2 optical images (F606W and F814W), as these wavelengths are less affected by dust extinction, and using the galaxy features visible in both bands to align them. For these objects (Circinus, ESO 137-G34, ESO 362-G8, NGC 1672, NGC 2639, NGC 5194, NGC 5256, NGC 5728, NGC 6300, and NGC 6951) a precision of a few ACS pixels was achieved, and that was enough for the rest of the analysis, so the inner regions are qualitatively described by the profiles.

The PSF of the instrumental configuration was computed with the software TinyTim.[10] The resulting PSF was compared with the radial profiles of several isolated stars in some images, showing a very good agreement. We then compared the PSF with the surface brightness profiles in order to determine whether or not the galaxies show a compact resolved nucleus. The PSF of the ACS HRC at this wavelength has a 1.8 pixel FWHM, so a compact source with a FWHM larger than 0.05″ should be seen slightly extended. The occurrence of a nuclear point source was determined by visual inspection of the radial profiles overplotted, in a

[10] See http://www.stsci.edu/software/tinytim/tinytim.html.

TABLE 3
FREQUENCY OF POINTLIKE NUCLEI

Sy Type	No Nucleus or Resolved	Unresolved	At Resolution Limit	Total
Sy2	43 (91.5%)	3 (6.4%)	1 (2.1%)	47
Sy1.8–1.9	5 (35.7%)	5 (35.7%)	4 (28.6%)	14
Sy1–1.5	0	14 (100%)	0	14
Total	48	22	5	75

NOTES.—The table shows the number of objects of each type for which we resolve the nucleus. The numbers in parentheses are the equivalent percentages relative to the total number of objects of each type. Note that no Sy1 nucleus is resolved.

logarithmic scale, on the PSF profile and normalized to the same peak value. The results are summarized in Table 3. This table shows the number of objects of each Seyfert type for which the ACS HRC shows a compact and unresolved nucleus. We have not found resolved nuclei in any galaxy from type Sy1 to Sy1.5. On the other hand, most Sy2 nuclei appear resolved or absent (heavily obscured). For the intermediate types 1.8–1.9 the situation is something in between, with approximately one-third of the nuclei resolved, one-third remaining pointlike, and the rest being difficult to discern. The objects with nuclei at the limit of resolution are Mrk 516, Mrk 334, NGC 4565, UGC 1395, and the Sy2 CGCG 164–019. This result is similar to that obtained at other wavelengths; for example, Nelson et al. (1996) show that in the red, Sy2's in general lack a compact nucleus, while Sy1–1.5 galaxies are dominated by a bright unresolved nuclear source.

The computed profiles are shown in Figure Set 9. By inspection of these plots we have classified the surface brightness profiles into one of these three categories:

Exponential.—The differential flux has an exponential dependence on the radius, so the dependence of the surface brightness (μ) is linear with r. This is the classical model to fit well the surface brightness profile of some dwarf ellipticals and the disks of spiral galaxies (Freeman 1970).

de Vaucouleurs profile.—This is an $r^{1/4}$ profile. This is a good approximation to the large-scale profiles of bright ellipticals and the bulges of spirals.

Nuker law.—This is a five-parameter model proposed by Lauer et al. (1995) that is a blend of two power laws. The Nuker law is used to fit the inner parts of the galactic profiles.

Some of the galaxies are a clear example of a particular profile: e.g., NGC 5283, follows a perfect de Vaucouleurs law; ESO 362-G8 matches a Nuker law; and NGC 4725 shows a Nuker law within the inner 2″ and a clear exponential in the outer regions. However, less than half of the objects show a correspondence with these profiles. More complex profiles are due to the effects of dust obscuration, occurrence of star-forming regions, or the presence of a bright nucleus, which can dominate the profile up to 2″. NGC 5194 is an example of central dust obscuration, while NGC 5135 shows an irregular profile due to its nuclear starburst. The profiles can show as well the presence of a ringlike structure, as in NGC 4303 or NGC 7496. The objects whose nucleus is obscured in the UV images show a very irregular profile. The classification of the profiles is shown in the last column of Table 4.

3.2. *Photometry*

The differential surface brightnesses were obtained by calculating the flux within a very narrow circular annulus, dividing it by the area of the region, and then calculating the magnitude. From the luminosity profiles and the background, we can define the maximum radius ($R_{\max}$) as the distance from the center at which the differential surface brightness equals the background value plus 1 σ. We consider that this criterion limits the region in which the flux can be calculated with enough S/N, and thus, it gives an idea of the extent of the object. We have calculated the magnitude inside apertures of radii $R_{\max}$, 1″, and 0.3″. The last two enclose, respectively, 94% and 86% of the total flux for a pointlike source. Also, we have calculated the absolute magnitudes inside apertures of projected radii equal to 100 and 300 pc. All the magnitudes are calculated in the STMAG system, with the formula

$$m = -2.5 \log\left[(\text{counts s}^{-1})\text{PHOTFLAM}\right] - 21.1,$$

where PHOTFLAM is the inverse sensitivity (see Pavlovsky et al. [2004] for an explanation of the STMAG system and the calculation of the zero point).

For some objects that are too extended, $R_{\max}$ is larger than the distance from the nucleus to the border of the image, and thus, it cannot be calculated with the standard procedure. We then take an alternative maximum radius that fits inside the field of view but does not include the borders of the image, where the data do not have enough quality. This is the case for NGC 3031, NGC 5941, and NGC 5005, in which $R_{\max}$ becomes a lower limit, and thus also affects the other measurements of size and magnitude. Note also that since $R_{\max}$ is calculated with an azimuthal average, some emitting features or isolated star-forming regions may fall outside the region we are studying.

We also calculate the differential surface brightness at 0.3″ and 1″ ($\mu_{0.3''}$, $\mu_{1''}$), as well as at the half-light radius (radius enclosing half of the total flux, or μ_{50}), and the radii enclosing 80%, 50%,

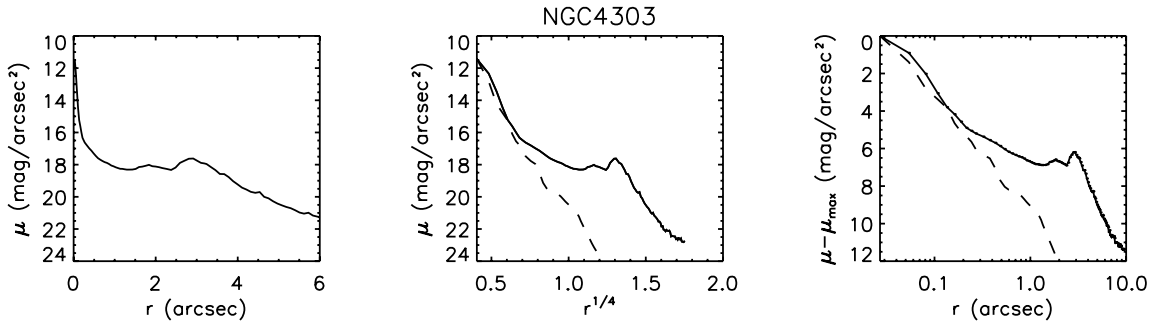

FIG. 9.51. Surface Brightness Profile of NGC 4303.

FIG. SET 9.—Surface brightness profiles for all the galaxies in the sample. From left to right, the abscissae are scaled linearly, with $r^{1/4}$, and logarithmically, in order to show the type of profile dominating in each galaxy (exponential, de Vaucouleurs, or Nuker law). Theoretical PSF profiles are overplotted with the dashed line for comparison with each object. [*See the electronic edition of the Journal for* Figs. 9.1–9.75.]

TABLE 4

MEASUREMENTS AND RESULTS

Galaxy Name (1)	$m(0.3'')$ (2)	$m(1'')$ (3)	$m(R_{max})$ (4)	$M(100\ pc)$[a] (5)	$M(300\ pc)$[a] (6)	$\mu(0.3'')$ (7)	$\mu(1'')$ (8)	μ_{50} (9)	R_{max} (pc) (10)	R_{80} (pc) (11)	R_{50} (pc) (12)	R_{20} (pc) (13)	Profile (14)
CGCG 164−019	17.66	17.05	16.47	−17.50	−17.96	17.98	19.48	19.39	1586 (2.74)	1013 (1.75)	439 (0.76)	52 (0.09)	v
Circinus	14.12	11.88	9.71	...	...	12.93	13.29	13.43	62 (3.23)	53 (2.77)	40 (2.12)	24 (1.27)	0
ESO 103-G35	19.79	18.06	17.01	−14.20	−15.79	18.93	19.69	19.92	578 (2.25)	475 (1.85)	315 (1.23)	157 (0.61)	n
ESO 137-G34	19.83	17.21	16.11	−14.55	−16.47	18.36	18.77	18.82	354 (1.99)	299 (1.68)	221 (1.24)	123 (0.69)	0
ESO 138-G1	16.4	15.43	15.09	−17.00	−17.62	15.56	18.11	16.92	390 (2.20)	216 (1.22)	95 (0.54)	37 (0.21)	np
ESO 362-G8	17.66	15.85	14.34	−16.50	−18.13	16.51	17.70	18.97	1906 (6.17)	1307 (4.23)	659 (2.13)	256 (0.83)	n
Fairall 49	18.03	16.75	15.98	−16.38	−17.49	17.66	18.73	18.74	930 (2.37)	604 (1.54)	398 (1.01)	165 (0.42)	er
IC 2560	16.91	16.36	16.02	−16.33	−16.81	16.75	19.28	17.32	409 (2.16)	231 (1.22)	72 (0.38)	21 (0.11)	0
IC 4870	15.54	15.34	14.48	−15.23	...	17.2	18.84	19.05	283 (4.96)	192 (3.37)	78 (1.37)	<3 (0.05)	enp
IC 5063	19.23	17.9	15.81	−14.47	−15.85	18.74	19.66	19.92	876 (3.98)	722 (3.28)	507 (2.30)	277 (1.26)	e
Mrk 6	14.85	14.67	14.57	−19.53	−19.68	16.31	18.79	11.32	732 (2.00)	139 (0.38)	<24 (0.07)	<11 (0.03)	np
Mrk 40	16.99	16.72	16.58	−17.61	−17.83	18.22	20.30	14.52	691 (1.69)	274 (0.67)	38 (0.09)	<12 (0.03)	np
Mrk 42	15.92	15.67	15.55	−19.01	−19.14	17.8	18.57	12.35	796 (1.67)	348 (0.73)	<32 (0.07)	<14 (0.03)	0pr
Mrk 231	14.54	14.43	14.18	−21.44	−21.61	16.57	18.88	11.02	3749 (4.59)	931 (1.14)	<55 (0.07)	<25 (0.03)	vp
Mrk 334	17.05	16.31	15.32	−17.59	−18.19	17.61	18.96	19.91	1760 (4.14)	1309 (3.08)	700 (1.65)	119 (0.28)	0
Mrk 461	15.88	15.58	15.13	−18.24	−18.51	16.5	19.16	16.47	1133 (4.32)	590 (2.25)	77 (0.30)	21 (0.08)	0r
Mrk 471	19.58	18.49	16.28	−15.76	−16.39	19.57	20.07	20.75	2758 (4.16)	2400 (3.62)	1741 (2.63)	922 (1.39)	0p
Mrk 477	16.5	16.03	15.44	−19.42	−19.84	16.61	19.13	18.32	1080 (3.44)	703 (2.24)	203 (0.64)	41 (0.13)	0
Mrk 493	14.71	14.5	14.43	−20.50	−20.66	16.58	18.55	11.49	1153 (1.90)	261 (0.43)	<44 (0.07)	<18 (0.03)	0pr
Mrk 516	18.54	17.83	17.14	−16.07	−17.11	17.7	20.23	20.17	1185 (2.15)	865 (1.57)	509 (0.92)	127 (0.23)	0
Mrk 915	15.11	14.94	14.79	−19.71	−19.85	16.89	18.81	11.57	1137 (2.43)	262 (0.56)	<30 (0.06)	<14 (0.03)	0p
Mrk 1210	16.54	16.11	15.4	−16.76	−17.24	16.94	19.20	19.04	2866 (3.92)	2047 (2.80)	667 (0.91)	73 (0.10)	0r
NGC 449	17.45	16.95	16.51	−16.63	−17.06	17.31	20.02	18.33	699 (2.26)	467 (1.51)	133 (0.43)	34 (0.11)	0
NGC 1144	19.81	18.22	16.26	−14.87	−16.29	18.91	20.07	21.67	2851 (5.10)	2622 (4.69)	2029 (3.63)	688 (1.23)	0
NGC 1320	17.64	16.92	15.39	−15.48	−16.30	17.61	19.24	20.14	893 (5.19)	702 (4.08)	419 (2.43)	127 (0.74)	v
NGC 1672	18.78	16.42	12.39	−15.08	−17.28	17.41	17.92	17.69	875 (10.18)	587 (6.83)	423 (4.92)	280 (3.25)	0
NGC 2639	19.32	17.47	15.04	−14.70	−16.21	18.06	19.28	20.19	1326 (6.14)	1084 (5.02)	705 (3.26)	352 (1.63)	n
NGC 3031[bc]	15.79	15.07	17.48	−14.90	...	16.34	17.23	18.54	>185 (10.85)	145 (8.52)	93 (5.45)	43 (2.52)	ep
NGC 3081	17.76	16.58	14.71	−15.33	−16.54	17.41	18.50	20.34	979 (6.36)	788 (5.12)	489 (3.17)	174 (1.13)	0
NGC 3227	14.46	14.27	14.05	−16.74	...	15.85	18.16	12.11	283 (3.79)	65 (0.87)	8 (0.10)	<2 (0.03)	0p
NGC 3362	19.22	18.35	16.52	−15.64	−16.45	19.01	20.77	21.79	2615 (4.88)	2385 (4.45)	1781 (3.32)	600 (1.12)	nr
NGC 3393	18.67	16.75	14.95	−15.35	−17.08	17.46	18.30	18.66	1135 (4.69)	784 (3.24)	466 (1.93)	249 (1.03)	n
NGC 3486	18.05	17.14	15.7	−13.25	...	17.95	19.31	19.95	148 (4.12)	116 (3.23)	72 (1.99)	26 (0.71)	e
NGC 3516	13.67	13.51	13.11	−19.15	−19.35	15.54	17.39	12.04	1014 (5.93)	347 (2.03)	20 (0.11)	<5 (0.03)	np
NGC 3786	17.07	16.37	15.96	−16.03	−16.70	17.32	18.60	18.33	381 (2.20)	220 (1.27)	104 (0.60)	14 (0.08)	0
NGC 3982	18.44	17.44	15.38	−13.94	−15.14	18.75	19.35	20.61	524 (6.39)	436 (5.32)	263 (3.21)	107 (1.30)	0
NGC 4253	15.61	15.3	14.75	−17.98	−18.27	16.41	18.69	17.31	1199 (4.89)	684 (2.79)	115 (0.47)	15 (0.06)	np
NGC 4258	17.86	15.92	13.2	−15.02	...	16.78	17.49	18.38	205 (6.20)	163 (4.93)	112 (3.39)	59 (1.79)	en
NGC 4303	16.19	15.56	13.54	−16.03	−17.50	16.61	18.02	17.60	558 (5.52)	361 (3.57)	277 (2.74)	141 (1.40)	0pr
NGC 4395	16.77	16.57	16.5	...	...	17.43	20.78	14.40	22 (1.43)	5 (0.32)	2 (0.10)	<1 (0.04)	0
NGC 4565	19.91	18.27	17.16	−13.18	...	19.14	19.86	20.00	181 (2.26)	144 (1.80)	100 (1.25)	52 (0.65)	0
NGC 4593	13.33	13.22	13.03	−19.51	−19.63	15.35	17.64	9.64	813 (4.67)	87 (0.50)	<11 (0.06)	<5 (0.03)	0p
NGC 4725	18.26	16.58	14	−14.80	−16.23	17.31	18.29	19.64	651 (8.35)	496 (6.36)	313 (4.02)	144 (1.84)	e
NGC 4939	18.98	17.08	16.27	−14.99	−16.33	18.06	19.21	19.44	553 (2.75)	410 (2.04)	215 (1.07)	103 (0.51)	v
NGC 4941	18.02	16.93	15.58	−14.26	...	17.26	18.95	19.60	279 (3.87)	211 (2.93)	128 (1.78)	48 (0.67)	e
NGC 5005[b]	18.15	16.38	22.32	−15.22	−16.54	17.06	18.11	20.00	>1252 (12.15)	1049 (10.18)	730 (7.09)	333 (3.23)	ev

TABLE 4—*Continued*

Galaxy Name (1)	$m(0.3'')$ (2)	$m(1'')$ (3)	$m(R_{max})$ (4)	M(100 pc)[a] (5)	M(300 pc)[a] (6)	$\mu(0.3'')$ (7)	$\mu(1'')$ (8)	μ_{50} (9)	R_{max} (pc) (10)	R_{80} (pc) (11)	R_{50} (pc) (12)	R_{20} (pc) (13)	Profile (14)
NGC 5033	16	15.64	13.65	−15.77	−16.45	17.04	18.58	20.14	1060 (11.64)	844 (9.27)	520 (5.72)	148 (1.63)	np
NGC 5135	16.49	15.4	13.59	−17.39	−18.52	16.08	17.47	17.44	1721 (6.47)	1064 (4.00)	470 (1.77)	277 (1.04)	0
NGC 5194[bc]	17.73	15.34	13.44	−14.74	−15.83	16.09	17.56	19.73	>340 (9.18)	277 (7.48)	173 (4.67)	38 (1.03)	0
NGC 5256	17.07	16.54	16.11	−17.81	−18.51	16.86	19.79	17.42	1468 (2.72)	896 (1.66)	223 (0.41)	70 (0.13)	0
NGC 5273	15.29	15.02	14.65	−16.32	−16.71	16.83	18.41	17.19	388 (3.76)	162 (1.57)	43 (0.41)	<3 (0.03)	np
NGC 5283	18.24	16.92	16	−15.45	−16.57	17.34	18.96	19.13	582 (2.88)	418 (2.07)	237 (1.18)	91 (0.45)	v
NGC 5347	18.13	17.15	16.88	−15.00	...	17.79	19.80	18.51	267 (1.76)	159 (1.05)	83 (0.55)	24 (0.16)	0
NGC 5548	14.31	14.17	13.98	−19.87	−20.00	15.93	18.35	10.84	1213 (3.65)	216 (0.65)	<22 (0.07)	<10 (0.03)	0p
NGC 5674	18.05	16.97	16.61	−16.65	−17.65	17.63	19.67	18.32	966 (2.00)	599 (1.24)	292 (0.60)	97 (0.20)	0
NGC 5695	19.11	17.6	16.6	−14.90	−16.26	18.18	19.48	19.94	767 (2.81)	584 (2.14)	344 (1.26)	147 (0.54)	v
NGC 5728	21.1	17.52	14.42	−13.67	−16.35	19.48	18.69	19.22	1148 (6.38)	846 (4.70)	656 (3.64)	369 (2.05)	0r
NGC 5940	15.43	15.31	15.26	−20.12	−20.28	17.36	19.74	11.63	1042 (1.59)	118 (0.18)	<40 (0.06)	<20 (0.03)	0p
NGC 6300	21.1	18.62	17.62	−12.81	...	19.6	19.99	20.00	123 (1.77)	106 (1.53)	78 (1.13)	46 (0.67)	0
NGC 6814	13.25	13.13	13.02	−18.27	...	15.26	17.47	9.93	279 (2.79)	25 (0.25)	<7 (0.07)	<3 (0.03)	0p
NGC 6951	18.23	16.9	13.74	−14.60	−16.55	17.25	18.73	18.64	474 (5.15)	417 (4.53)	344 (3.74)	222 (2.41)	0r
NGC 7130	15.98	15.17	13.47	−18.13	−18.87	15.53	18.64	20.04	3333 (10.65)	2601 (8.31)	1908 (6.09)	266 (0.85)	0
NGC 7212	18.03	17.19	16.43	−16.47	−17.59	17.2	19.53	19.54	1310 (2.54)	980 (1.90)	518 (1.00)	134 (0.26)	0
NGC 7319	20.51	18.91	18.91	−14.05	−15.41	20.15	20.86	19.84	441 (1.01)	349 (0.80)	247 (0.57)	109 (0.25)	0
NGC 7469	13.22	13.08	12.65	−20.85	−20.98	15.14	16.85	11.83	1376 (4.35)	506 (1.60)	39 (0.12)	<9 (0.03)	0pr
NGC 7479	19.56	18	16.89	−14.01	−15.34	18.49	19.91	20.05	367 (2.38)	310 (2.01)	205 (1.33)	89 (0.58)	0
NGC 7496	16.48	15.43	14.35	−16.23	−17.18	15.75	17.55	17.40	538 (5.02)	272 (2.54)	143 (1.33)	45 (0.42)	0
NGC 7674	16.47	15.89	15.69	−18.52	−19.16	16.4	18.89	16.48	1082 (1.93)	510 (0.91)	177 (0.32)	50 (0.09)	n
NGC 7743	17.22	16.01	15.04	−15.71	−16.48	16.38	18.41	18.90	463 (4.18)	316 (2.85)	152 (1.37)	48 (0.43)	n
UGC 1214	17.44	16.51	15.41	−16.75	−17.60	16.85	18.87	19.43	1333 (3.99)	945 (2.83)	522 (1.56)	137 (0.41)	n
UGC 1395	18.52	17.35	17.26	−15.69	−16.79	18.4	20.06	18.46	381 (1.23)	270 (0.80)	177 (0.52)	40 (0.12)	0
UGC 2456	16.53	15.85	15.36	−17.11	−17.76	15.84	18.31	17.75	598 (2.57)	333 (1.43)	143 (0.61)	44 (0.19)	0
UGC 6100	18.84	17.84	16.63	−15.94	−16.99	18.28	20.11	21.03	2219 (3.88)	1830 (3.20)	1022 (1.79)	297 (0.52)	n
UGC 12138	14.96	14.73	14.62	−19.98	−20.19	16.38	18.88	11.64	1054 (2.18)	232 (0.48)	<34 (0.07)	<15 (0.03)	np
UM 625	17.44	16.35	16.15	−17.39	−18.29	17.53	19.39	17.37	887 (1.83)	436 (0.90)	252 (0.52)	53 (0.11)	0

NOTES.—Col. (1): Galaxy name. Col. (2): Magnitude within 0.3″ radius. Col. (3): Magnitude within 1″ radius. Col. (4): Magnitude within the maximum radius. Col. (5): Absolute magnitude within a projected radius of 100 pc. Col. (6): Absolute magnitude within 300 pc. Cols. (7), (8): Differential surface brightness at 0.3″ and 1″, respectively. Col. (9): Differential surface brightness at the half-light radius. Col. (10): Computed maximum radius in parsecs. The value in parentheses is in arcseconds. Cols. (11)–(13): Radius enclosing 80%, 50%, and 20% of the flux within R_{max}, in parsecs. The value in parentheses is in arcseconds. Col. (14): Classification of the profiles from Fig. Set 9. The type of profile is coded with the letters "e" for an exponential profile, "v" for a de Vaucouleurs law, "n" when a Nuker law is seen, and "0" if the profile does not fall in any of the former categories. A letter "p" is added when there is a pointlike nucleus present, and an "r" if there is a ring visible in the image. All the magnitudes are calculated in the STMAG system and corrected for Galactic extinction.

[a] In the cases in which R_{max} is less than 100 pc, the absolute magnitude (M) within 300 or 100 pc is not calculated. If R_{max} is less than 300 pc but greater than 100 pc, then M within 300 pc is computed, but not M within 100 pc.

[b] In these cases R_{max} is limited by the border of the field of view and not by the integration.

[c] Occulting finger of the HRC limits the radius for which the asymmetry parameter (see text) is computed (smaller than R_{max}).

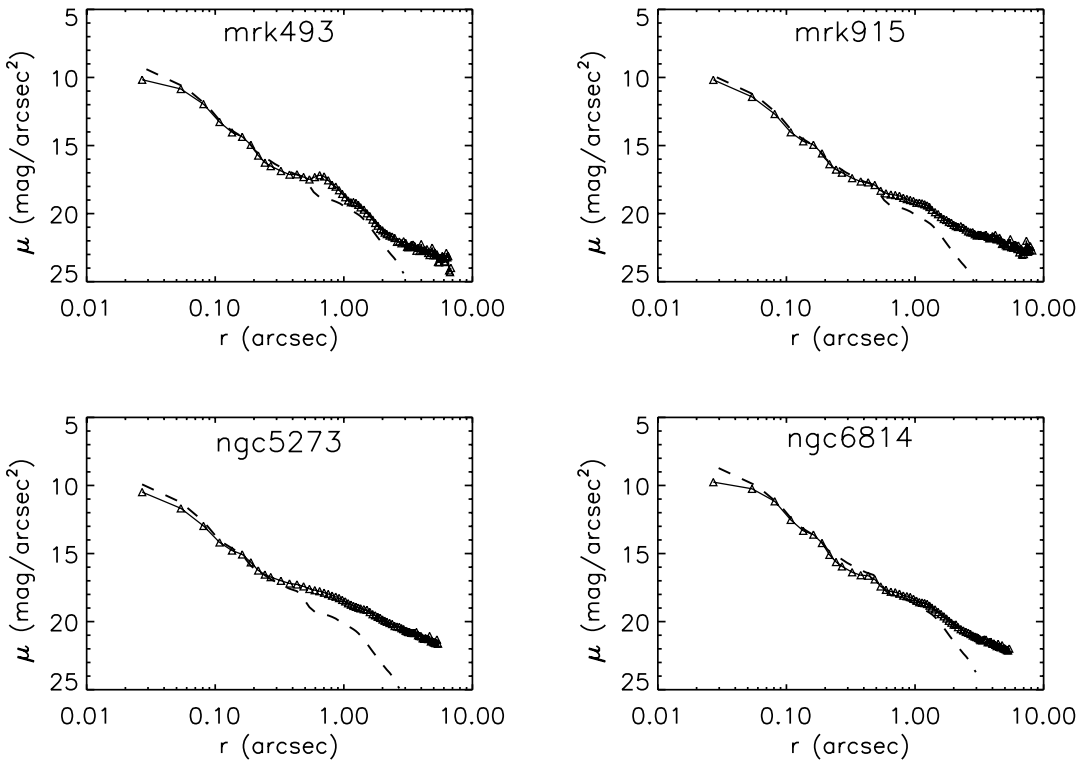

FIG. 10.—PSF fit to the nucleus for the saturated objects with two images. The fitted PSF is the dashed line, overplotted on the surface brightness curve (*black line and triangles*), for each object. The most affected nucleus is NGC 6814, while Mrk 915 has barely lost flux in the saturated image. [*See the electronic edition of the Journal for a color version of this figure.*]

and 20% of the total flux (R_{80}, R_{50}, and R_{20}). We have obtained that for several objects half or more of the flux is enclosed within a radius of 1 pixel. For these objects (all the Sy1's and some intermediate-type Seyfert galaxies), which exhibit a bright point-like nucleus, we can only set an upper limit for R_{50} and R_{20}. All the magnitudes are then corrected for Galactic reddening using the extinction coefficients given in Sirianni et al. (2005), which are calculated using the extinction law of Cardelli et al. (1989). The correction for a particular filter depends on the shape of the continuum. We have used $A(\mathrm{F330W})/E(B-V) = 5.054$, that is, an average of the values given for Sc and elliptical galaxies in Sirianni et al. (2005). The photometry results are given in Table 4.

As explained above, saturation might affect the fluxes in some nuclei. This effect can be corrected straightforwardly for the objects overcoming the saturation threshold which also have short-exposure images. First we checked that from a radius of 0.1″ outward, the surface brightness profiles calculated from both images were coincident. Then the inner 8 pixels of the saturated and high-S/N image were replaced by the data from the unsaturated image. The final analysis was carried out on this corrected profile. For the saturated objects with just one image we performed a χ^2 fit of a TinyTim-generated PSF to the wings of the nuclear PSF. The fit was done in the range of 5–12 pixels (0.13″–0.32″), the range in which the pixels are not severely affected by the saturation and the S/N is still high. We considered possible focus changes by allowing the PSF to be broadened up to 10%, choosing the best fit from the whole set of different broadenings. The inner 0.2″ of the galaxy was replaced by the fitted PSF. We checked this method with those core-saturated galaxies which had additional nonsaturated exposures, obtaining a good agreement with the fluxes calculated from the combined profiles. Figure 10 shows the fitted PSFs for these four nuclei. The resulting corrections calculated range from 0.06 mag (Mrk 915) to 0.36 mag (NGC 5273). The nucleus of NGC 5940 does not reach the saturation threshold, but it is close to it. It has only a long-exposure image, in which it does not seem to be affected by saturation. The correction that we expect for this object should be smaller than that for Mrk 493 or Mrk 915, which have brighter nuclei.

The magnitudes given in Table 4 depend on the determination of $R_{\max}$, so one has to take this into account when using these fluxes. In order to illustrate this we have compared the total fluxes of some of our galaxies with the fluxes presented in Storchi-Bergmann et al. (1995) and Kinney et al. (1993). The compared subsamples are NGC 3982, NGC 4258, NGC 5005, NGC 5256, NGC 5674, and Mrk 477, which have been studied by Kinney et al. (1993) and have published fluxes at ∼2700 Å and spectral slopes (β); and the subsample NGC 3081, NGC 3393, NGC 5135, NGC 5728, NGC 1672, NGC 7130, and NGC 7496, which have been studied as well by Storchi-Bergmann et al. (1995), giving fluxes at 2900 and 3500 Å. Figure 11 shows the comparison between their measurements and ours. A good general agreement is found. When comparing the fluxes several issues have to be taken into account, with the different instrumental setups being the most important. In order to have a good S/N we have measured inside a radius $R_{\max}$, while they used the aperture of the *IUE* slit, which is 10″ × 20″. This is equivalent in surface to a circular aperture of 8″, although the flux depends on the light distribution of the object and the orientation of the slit. Thus, when we use apertures of 8″ the agreement is very good, except for NGC 4258 and NGC 5005, for which we measure a flux 1.9 and 2.5 times higher, respectively. In these cases the isophotes are clearly elongated, so the flux is expected to vary significantly with the slit orientation. Moreover, because the calculation of $R_{\max}$ implies an azimuthal average, some bright features can lie out of this region. One example of this is NGC 5674, which has an external ringlike structure which is outside of $R_{\max}$ but fits in an 8″ aperture. The

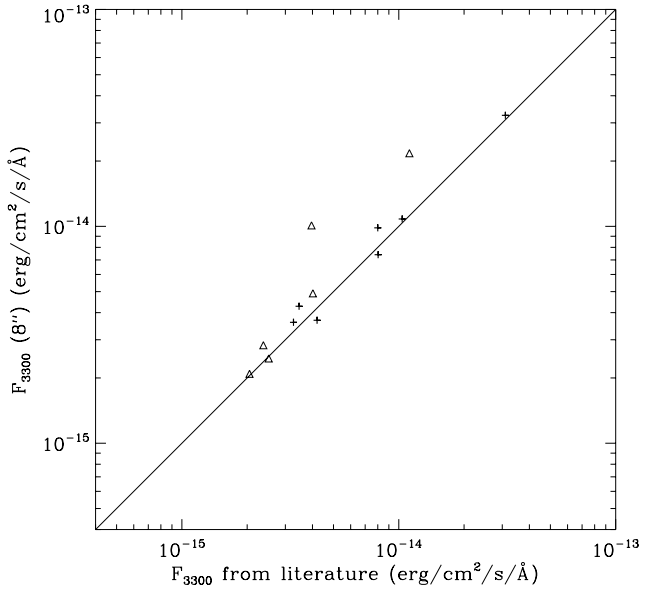

FIG. 11.—Comparison of the fluxes that we have measured with data from the literature. Triangles represent fluxes from Kinney et al. (1993), while crosses represent fluxes from Storchi-Bergmann et al. (1995). The two triangles that fall over the unity line are NGC 4258 and NGC 5005 (see discussion in text).

fluxes at 3300 Å have been interpolated between the fluxes at 2900 and 3500 Å given by Storchi-Bergmann et al. (1995), or corrected from the fluxes at 2700 Å given by Kinney et al. (1993) using the value of β that they calculate. In Table 5 we list the calculated photometric values for these objects.

Figure 12 presents comparative histograms of the values of the magnitudes measured within 0.3″, 1″, and R_{max}, and in a circular ring between 0.3″ and 1″. It is shown that Sy1 nuclei are brighter at small radii. However, this trend is not observed when the contribution of the inner 0.3″ is subtracted, indicating that the light in Sy1's is dominated by the compact nucleus, and the difference of the subsamples in terms of magnitude is not large.

TABLE 5
COMPARISON OF FLUX MEASUREMENTS

Name (1)	R_{max} (arcsec) (2)	$F_{3300}(R_{max})$ (3)	$F_{3300}(8'')$ (4)	$F_{3300}(10'' \times 20'')$ (5)
Mrk 477[a]	3.4	2.3	2.8	2.4
NGC 1672	10.2	36.2	32.5	31.0
NGC 3081	6.4	3.7	4.3	3.5
NGC 3393	4.7	2.7	3.6	3.3
NGC 3982[a]	6.4	3.1	4.9	4.0
NGC 4258[a]	6.2	13.0	21.7	11.2
NGC 5005[a]	12.2	17.0	10.1	4.0
NGC 5135	6.5	10.0	10.8	10.4
NGC 5256[a]	2.7	1.2	2.5	2.5
NGC 5674[a]	2.0	0.7	2.1	2.1
NGC 5728	6.4	3.5	3.7	4.2
NGC 7130	10.7	13.0	9.8	8.0
NGC 7496	5.0	6.3	7.4	8.0

NOTES.—This table shows the comparison between our measurements and the values published by Kinney et al. (1993) and Storchi-Bergmann et al. (1995). Col. (1): Galaxy name. Col. (2): Maximum radius. Col. (3): UV flux measured at maximum radius. Col. (4): UV flux measured at 8″ radius. Col. (5): UV flux from the literature at 3300 Å. The units of cols. (3)–(5) are 10^{-15} ergs s^{-1} cm^{-2} Å^{-1}.

[a] The fluxes in col. (5) have been calculated using the spectral slope given in Kinney et al. (1993) for these galaxies.

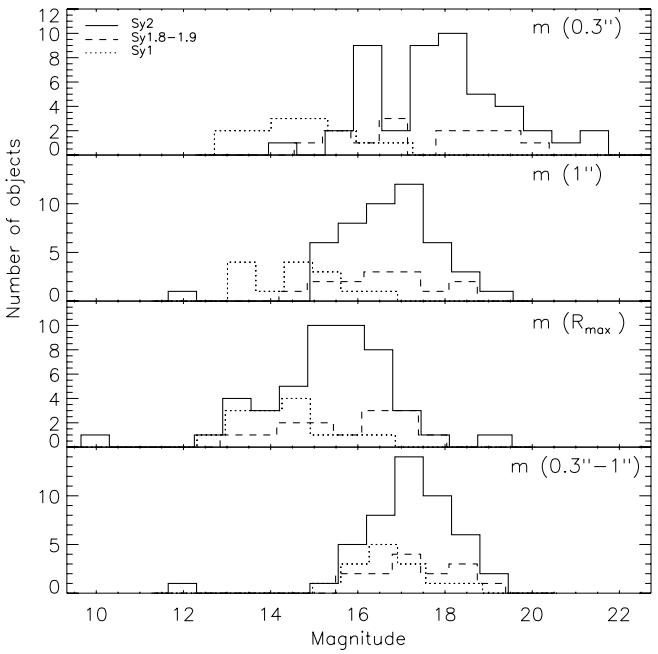

FIG. 12.—Comparative histogram of the magnitudes measured within different radii. Sy2's are plotted with the solid line; Sy1's with the dotted line; and Sy1.8–1.9 galaxies with the dashed line. Sy1 nuclei tend to be brighter than the others, although this trend is softened when larger radii are considered. The bottom panel shows the magnitude between 0.3″ and 1″ apertures. [*See the electronic edition of the Journal for a color version of this figure.*]

The bright outlier object in the plots is the Circinus galaxy, which due to its low Galactic latitude has a large extinction correction that makes it even brighter than the Messier objects of the sample. In Figure 13 we plot the surface brightness μ at 0.3″ and 1″. The calculation of the surface brightness at 1″ is practically unaffected by the Sy1 nuclei, which causes the dissimilarity between the panels of Figure 13. This indicates no significant difference among the hosts of Sy1's and Sy2's, in terms of surface brightness.

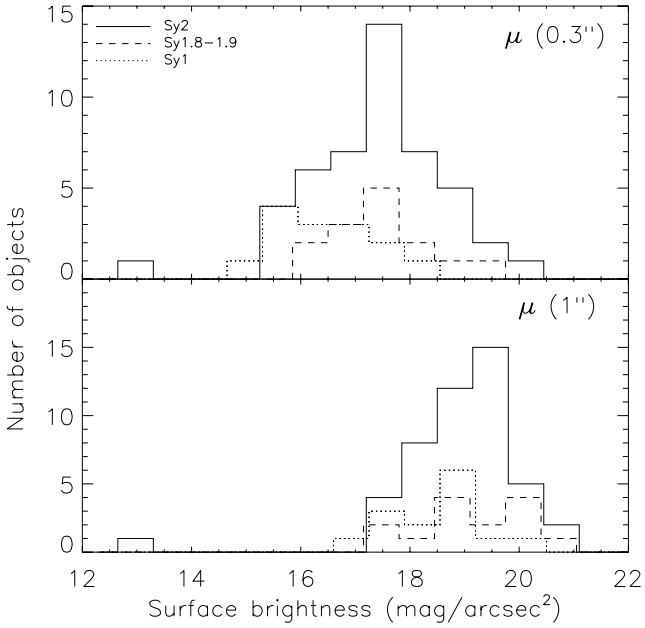

FIG. 13.—Comparative histogram of the values of the surface brightness measured at two different radii. At 0.3″ Sy1 nuclei are brighter than those from other types. At 1″, however, there is no difference in the distribution of μ. [*See the electronic edition of the Journal for a color version of this figure.*]

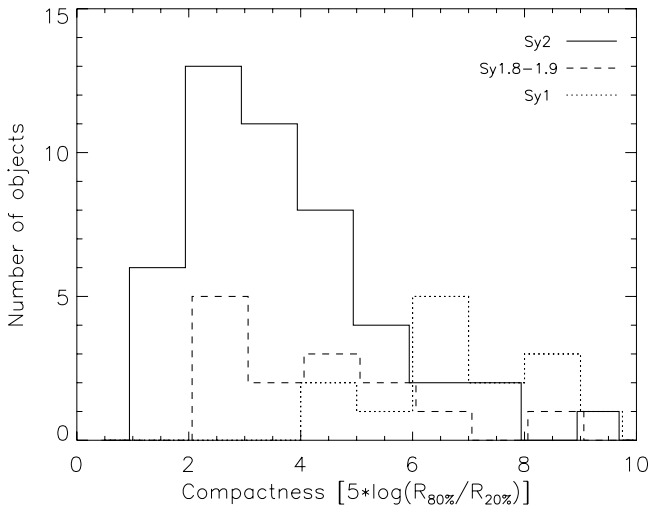

FIG. 14.—Histogram of compactness for Seyfert subsamples. The types of the lines codify the Seyfert types in the same way as in previous figures. [*See the electronic edition of the Journal for a color version of this figure*.]

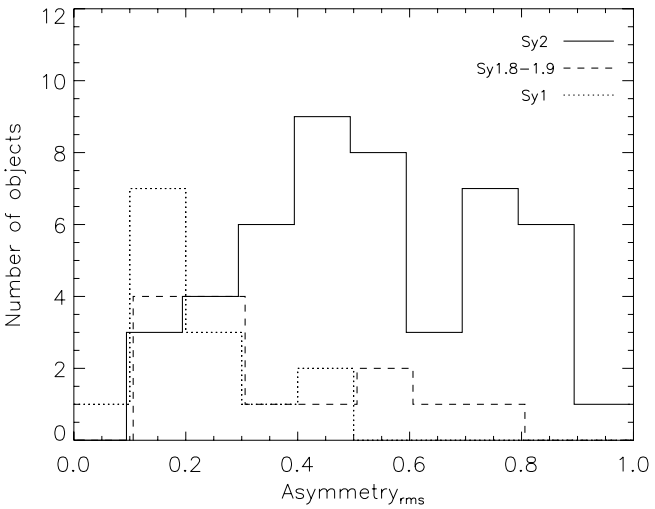

FIG. 15.—Histogram of asymmetry for Seyfert subsamples. The symbols are the same as in previous figures. [*See the electronic edition of the Journal for a color version of this figure*.]

The difference would be due just to the presence of the nuclear source in Sy1's.

3.3. *Compactness and Asymmetry*

The morphology of extended objects can be quantified with the concentration or compactness (C) and asymmetry (A) parameters. Due to the irregular distribution of light at 3300 Å, these parameters give a better description of the morphology than the classical bulge-disk decomposition. They also reflect the contribution of clumpy structure, such as star clusters and star-forming regions.

The definition of C is based on the curve of growth and depends on the ratio of two radii enclosing some fraction of the total flux. We have used the formula from Bershady et al. (2000),

$$C = 5 \log (r_{80}/r_{20}),$$

where r_{80} and r_{20} are the radii enclosing 80% and 20% of the total flux within $R_{\max}$. Figure 14 shows the distribution of C for the different types of Seyfert galaxies. The distribution of Sy2's and Sy1's are clearly different, with the Sy1's being far more compact. The intermediate types show a behavior in between the other two subsamples. We find that the values of C for Sy2's are similar to those of local normal galaxies studied in the B band by Bershady et al. (2000). However, our Sy1's have on average much higher values of C. The occurrence of a compact nucleus in the near-UV leads to a a high value of C measured at this wavelength.

The asymmetry of a particular galaxy is calculated by subtracting a 180° rotated image from the original one. The residuals in this image are summed up and then normalized, dividing by the total flux in the original image. The sum can be quadratic or in absolute value. The rotation center is the nucleus of the galaxy. The formula that summarizes the process is (Conselice 1997)

$$A^2_{\rm rms} = \frac{\sum (F_{ij} - F_{ji})^2}{2 \sum F^2_{ij}},$$

where F_{ji} is the rotated original image (F_{ij}). The value for A is calculated taking into account only the region inside $R_{\max}$; otherwise, the contribution of the noise would become important. In the cases of M81 and M51 we have measured only to a radius smaller than $R_{\max}$ (5.67″ for M81 and 6.91″ for M51), just enough to prevent the occulting "finger" of the ACS to enter into the region studied, which would introduce a big systematic uncertainty in the asymmetry determination (although this is unimportant for the photometry). We decided to use this definition of $A_{\rm rms}$ after trying out as well an absolute-value sum ($A_{\rm abs}$). In general, $A_{\rm rms}$ gives more weight to bright features, such as star-forming regions, and should be less sensitive to the noise. We have checked that the choice of the exact formula does not change the general results, as well as that measuring within a half-light radius does not change the general distribution of the points. Figures 15 and 16 show the histogram of $A_{\rm rms}$ values and an $A_{\rm rms}$ versus C plot. The values of $A_{\rm rms}$ for Sy2's are systematically higher, covering a wide range of values, while Sy1's show a very small scatter around $A_{\rm rms} = 0.2$. We calculated the asymmetry of some isolated pointlike sources leading to a value close to 0.2, so this seems to be a lower limit for the asymmetry calculated by this method. This is a combination of the contribution of the noise and subsampling effects due to the value of the PSF FWHM. Thus, $A_{\rm rms}$ is dominated by the nuclear PSF in Sy1's, while extended emission and star-forming regions, together with a

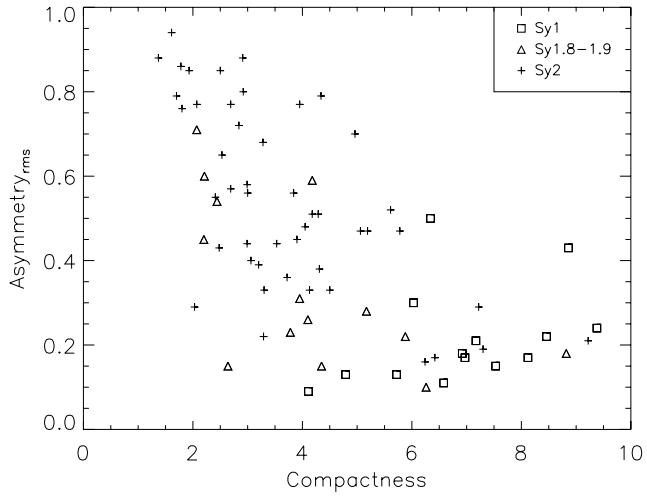

FIG. 16.—Asymmetry vs. compactness for the galaxies in the sample. Crosses stand for Sy2 galaxies, while triangles represent intermediate types. Sy1's are plotted with squares. [*See the electronic edition of the Journal for a color version of this figure*.]

TABLE 6

Results from the Shape and Stellar Cluster Analysis

Galaxy Name (1)	C (2)	A_{rms} (3)	f_{clus} (4)	$\log(f_{clus})$ (ergs cm^{-2} s^{-1} Å^{-1}) (5)
CGCG 164−019	6.42	0.17	0.022	−16.69
Circinus	1.7	0.79	0.016	−14.12
ESO 103-G35	2.41	0.55	0	...
ESO 137-G34	1.93	0.85	0.0058	−17.12
ESO 138-G1	3.84	0.56	0	...
ESO 362-G8	3.53	0.44	0	...
Fairall 49	2.84	0.72	0.033	−16.31
IC 2560	5.19	0.47	0	...
IC 4870[a]	>9.22	0.21	0.033	−15.71
IC 5063	2.07	0.77	0.014	−16.62
Mrk 6[a]	>5.72	0.13	0	...
Mrk 40[a]	>6.97	0.17	0	...
Mrk 42[a]	>7.17	0.21	0.038	−16.08
Mrk 231[a]	>8.12	0.17	0.009	−16.16
Mrk 334	5.17	0.28	0.13	−15.45
Mrk 461	7.3	0.19	0.0081	−16.58
Mrk 471	2.07	0.71	0.032	−16.45
Mrk 477	6.24	0.16	0	...
Mrk 493[a]	>6.03	0.30	0.034	−15.68
Mrk 516	4.18	0.59	0.033	−16.78
Mrk 915[a]	>6.58	0.11	0	...
Mrk 1210	7.22	0.29	0.016	−16.40
NGC 449	5.78	0.47	0.017	−16.81
NGC 1144	2.91	0.88	0.032	−16.44
NGC 1320	3.72	0.36	0	...
NGC 1672	1.61	0.94	0.13	−14.28
NGC 2639	2.44	0.54	0.0027	−17.02
NGC 3031[bc]	2.64	0.15	0	...
NGC 3081	3.28	0.68	0.078	−15.43
NGC 3227[a]	>7.53	0.15	0.003	−16.58
NGC 3362	2.99	0.58	0.04	−16.45
NGC 3393	2.48	0.43	0	...
NGC 3486	3.29	0.22	0	...
NGC 3516[a]	>9.38	0.24	0	...
NGC 3786	5.88	0.22	0.012	−16.74
NGC 3982	3.06	0.40	0.031	−16.10
NGC 4253	8.46	0.22	0.02	−16.04
NGC 4258	2.2	0.45	0.035	−15.18
NGC 4303	2.03	0.29	0.13	−14.74
NGC 4395[a]	>4.35	0.15	0.0093	−17.07
NGC 4565	2.21	0.60	0	...
NGC 4593[a]	>6.34	0.50	0.0023	−16.29
NGC 4725	2.69	0.57	0	...
NGC 4939	3	0.56	0.01	−16.95
NGC 4941	3.2	0.39	0.0087	−16.73
NGC 5005[b]	2.5	0.85	0.021	−19.05
NGC 5033	3.78	0.23	0.007	−16.05
NGC 5135	2.92	0.80	0.3	−14.40
NGC 5194[bc]	4.31	0.34	0.145	−14.65
NGC 5256	5.61	0.52	0.045	−16.23
NGC 5273[a]	>8.82	0.18	0.0056	−16.55
NGC 5283	3.3	0.33	0.063	−16.04
NGC 5347	4.05	0.48	0	...
NGC 5548[a]	>6.92	0.18	0.0055	−16.29
NGC 5674	3.95	0.31	0.11	−16.04
NGC 5695	2.99	0.44	0.039	−16.49
NGC 5728	1.8	0.76	0.04	−15.61
NGC 5940[a]	>4.11	0.09	0	...
NGC 6300	1.78	0.86	0	...
NGC 6814[a]	>4.79	0.13	0	...
NGC 6951	1.37	0.88	0.13	−14.82
NGC 7130	4.96	0.70	0.25	−14.43
NGC 7212	4.29	0.51	0.07	−16.17
NGC 7319	2.53	0.65	0.023	−17.64
NGC 7469[a]	>8.86	0.43	0.115	−14.44
NGC 7479	2.69	0.77	0.01	−17.20
NGC 7496	3.9	0.45	0.38	−14.60
NGC 7674	5.06	0.47	0.11	−15.67
NGC 7743	4.13	0.33	0	...
UGC 1214	4.18	0.51	0	...
UGC 1395	4.1	0.26	0	...
UGC 2456	4.34	0.79	0.3	−15.11
UGC 6100	3.95	0.77	0	...
UGC 12138[a]	>6.26	0.10	0	...
UM 625	4.5	0.33	0.1	−15.90

Notes.—Col. (1): Galaxy name. Col. (2): Compactness. Col. (3): Asymmetry. Col. (4): Fraction of light in stellar clusters. Col. (5): Logarithm of the total flux of light in clusters.

[a] These objects possess a very bright compact nucleus that affects the determination of R_{20} (see text). In these cases we can only set a lower limit for the compactness parameter.

[b] In these cases R_{max} is limited by the border of the field of view and not by the integration. Compactness and asymmetry are computed based on this smaller R_{max}.

[c] Occulting finger of the HRC limits the radius for which the asymmetry parameter (see text) is computed (smaller than R_{max}).

smaller nuclear contribution, determine the higher values in Sy2's. In Figure 16 it is clearly seen how Sy1.8–1.9 galaxies reproduce characteristics of both Seyfert types 1 and 2. In the plot A_{rms} versus C there is a clear trend that A_{rms} decreases with increasing C, as had been observed before for normal galaxies (see, e.g., Bershady et al. 2000). In this plot the correlation saturates when we explore high values of C, due to the limit in A_{rms}. Results of the calculation of C and A are summarized in Table 6.

3.4. *The Fraction of Light in Clusters*

In order to determine how important the contribution of star formation is to the total UV flux we have estimated which fraction of the total flux comes from stellar clusters or very compact light emission (f_{clus}), not including the compact Sy1 nuclei. Several software packages were used to detect the clusters. We found that in many cases the highly varying background, and the large dynamical range in some of the images, was a problem for these algorithms in giving a satisfying result. Also, the varied morphology became a problem when deciding a homogeneous and unbiased way to perform the analysis automatically. We sometimes obtained good results with the IRAF task DAOFIND, but it did not work well in crowded regions or with a highly varying background. Often we had to crop the resulting lists by hand and add some other objects. We thus decided to select the objects by visual inspection. To be sure that our selections were complete enough, we checked using linear and logarithmic displays, compared with the optical images in unclear cases, and compared with DAOFIND results. The selections were restricted to the region inside R_{max}, in which the total flux was measured, although sometimes there were obvious star clusters outside this region. See Figure 17 as an illustrative example. Note that not every clump was added but only the ones which seemed compact enough to be considered individual clusters or tight aggregations of them. Selecting the clusters by hand proved to be effective, although the limiting magnitude could not be determined due to the varying background. The completeness of the selection is not

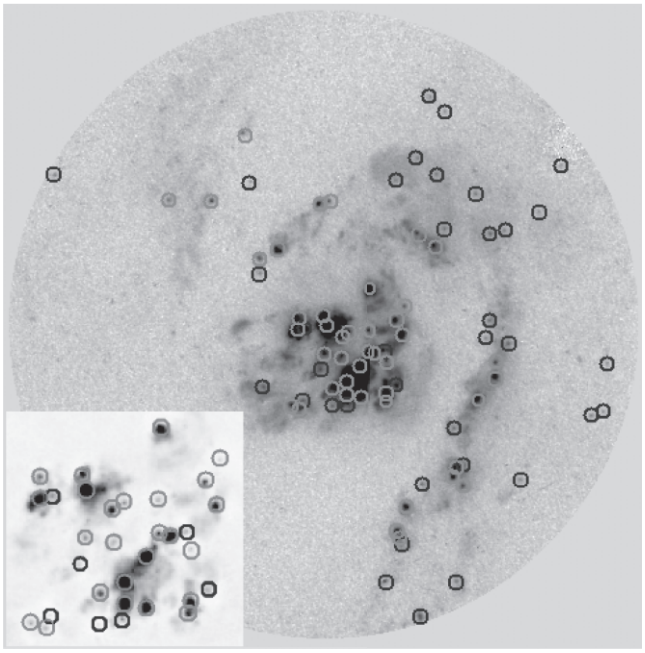

FIG. 17.—Example of the cluster selection for NGC 5135. Stellar clusters were identified combining a linear display to disentangle the brightest crowded regions (*gray circles*), and then using a logarithmic display, in order to identify the faint population (*black circles*). A close-up of the central region is shown in the lower left inset. [*See the electronic edition of the Journal for a color version of this figure*.]

critical for this work. Instead, we were interested in checking how robust the estimation of the flux in clusters was with respect to different star cluster selections. Wilson et al. (2006) study the star cluster population in Arp 220 with the ACS, finding the same problems. Manual cluster selection also proved to be efficient for them.

The flux determination was done with the IRAF task PHOT. We measured the flux within very small apertures, and then we applied aperture corrections from the enclosed energy curves of Sirianni et al. (2005). Using different apertures led to different results for $f_{\rm clus}$, in part due to the use of a correction for pointlike objects, when the star clusters may show a resolved structure, at least for large objects in nearby galaxies. However, in most objects the variation of $f_{\rm clus}$ when considering different apertures (at 3, 4, 5, or 6 pixel radius) was higher than the variation when using different selection methods. We therefore estimate that the main uncertainty source is the clustering of the objects and the highly varying background. Finally, we decided to use an aperture radius of 4 pixels, as a compromise between the sampling effects of a smaller aperture and the possible aperture overlapping of a larger one, which would also introduce a larger uncertainty in the background subtraction. The background was calculated by measuring in an annulus of 6 pixel inner radius and 2 pixel width in a median filtered image with a 15×15 pixel box. The fraction $f_{\rm clus}$ was then determined summing up the total flux in all the objects detected inside $R_{\rm max}$, local background subtracted and aperture corrected, and divided between the total flux within $R_{\rm max}$. In Table 6 we give $f_{\rm clus}$, as well as the logarithm of the total flux, in the star clusters.

In some galaxies we could not detect any star cluster inside the $R_{\rm max}$ aperture. This happened more often for Sy1's (6 out of 14 galaxies, or 43%) than for Sy2's (14 out of 47; 30%) or intermediate types (5 out of 14; 36%). Figure 18 shows a histogram of the distribution of $f_{\rm clus}$ for the galaxies with detected clusters.

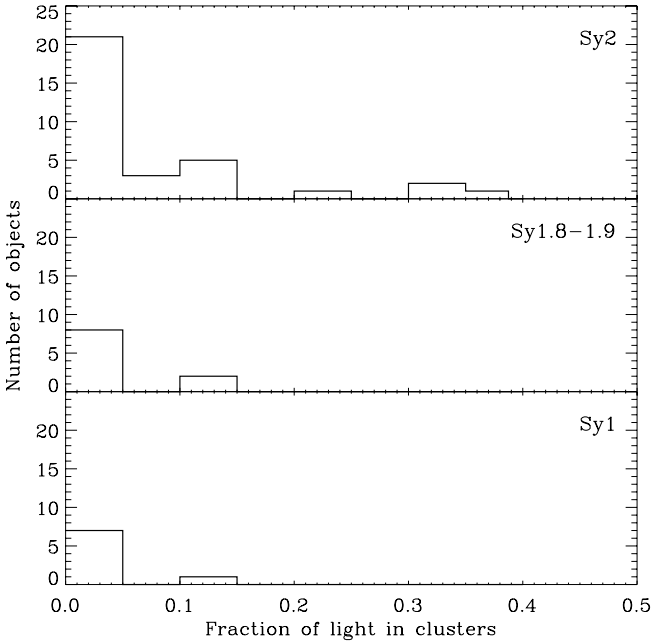

FIG. 18.—Histogram of $f_{\rm clus}$ for different Seyfert types. Only galaxies with detected star clusters have been included.

Except for Mrk 231, no Sy1's show stellar clusters or star-forming regions contributing more than 5% to the total flux, while there are 13 (∼28%) Sy2's that overcome this value. This confirms that Sy1 galaxies are core-dominated objects, while clusters and star formation account for a significant fraction of the light in Sy2's. This fraction is smaller than that calculated for UV-selected starburst galaxies, in which light from clumpy structure is, on average, on the order of 20% of the total flux (Meurer et al. 1995), although these results are for a different UV filter, at 2200 Å.

In order to directly compare the flux coming from clusters among the different subsamples, we plot in Figure 19 a comparative histogram of the total luminosity from stellar clusters. Despite the

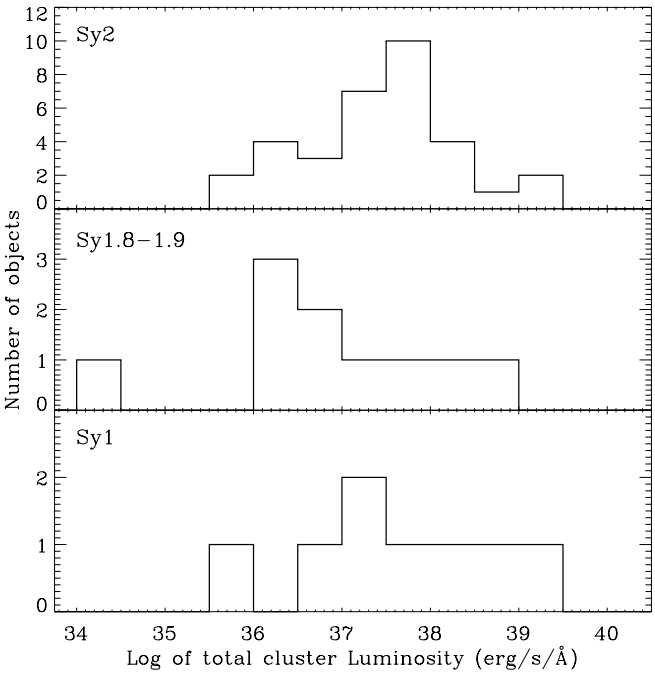

FIG. 19.—Histogram of the total luminosity coming from star clusters. The three distributions look quite similar.

small number of Sy1's and intermediate-type galaxies involved, this figure shows these sources to have a distribution of values similar to that of Sy2's. This suggests that these sources have similar amounts of recent star formation, confirming that most of the differences seen in Figure 18 are due to the strong contribution from the nuclear point source in the former.

We have shown that, in spite of the very high resolving power of *HST*, the bright Sy1 nuclei dominate the emission of the most inner near-UV morphology in this kind of galaxy. In order to unmask possible underlying star-forming regions, a very careful PSF subtraction for Sy1 nuclei is needed. Our team is currently working on this matter, and the results will be presented in a forthcoming paper (P. Spinelli et al. 2007, in preparation).

4. CONCLUSIONS

Using the high resolution of the Advanced Camera for Surveys on board *HST* we performed a snapshot survey of a sample of 75 nearby Seyfert galaxies in the near-UV. These observations complete a very useful multiwavelength database for these AGNs, which also have optical and near-IR images available in the *HST* archive. We have carried out a general analysis of the near-UV images of this sample, consisting of the identification of unresolved compact nuclear sources, extraction of surface brightness profiles, photometry, determination of compactness and asymmetry parameters, and identification of the star cluster population. The size of the sample allows us to compare the results of the analysis among different Seyfert types: Sy1 (including Sy1.2–1.5), Sy2, and intermediate types (Sy1.8–1.9).

The main conclusions from the photometric and morphological study are as follows:

1. In general, the morphology in the UV is very irregular, with clumpy and compact structure in most cases.

2. Sy1's are completely PSF-dominated objects in their inner regions, but Nuker law profiles are detected for some of the galaxies. Inspecting the surface brightness profiles we find 3 out of 14 Sy1 galaxies and 6 out of 47 Sy2 galaxies to posses a star-forming ring. On the contrary, no star-forming rings are found within the intermediate Seyfert type subsample. Sy2 galaxies present the most varied and irregular profiles. Some profiles follow an exponential, de Vaucouleurs, or Nuker law, but most of them cannot be easily classified.

3. No nucleus is resolved for any of the Sy1 objects, while on the other hand, almost all Sy2's have the nucleus resolved. At least 5 out of 14 Sy1.8–1.9 galaxies show an unresolved compact nucleus.

4. In terms of surface brightness at $1''$, and also from the calculation of the integrated magnitude between $0.3''$ and $1''$, we find no significant difference between the host galaxies of Sy1 and Sy2 nuclei. The difference would arise solely due to the presence of the nuclear source in Sy1's.

5. Sy1's are very compact and have low values of asymmetry, while Sy2's show a very wide range of compactness and asymmetry values.

From the study of the fraction of light in clusters we conclude the following:

1. Bright star clusters are slightly more often seen in Sy2's ($\sim$70%) than in Sy1's ($\sim$57%) or in intermediate Seyfert types ($\sim$64%). However, we have shown that this difference may be due to the masking of the inner regions by the contribution of the bright Seyfert 1 nuclei.

2. The distribution of the luminosity in star clusters does not change much among different Seyfert types when considering only galaxies with detected clusters.

3. The contribution of the clusters to the total flux is much more important in Sy2's (where it reaches up to 30%) than in the other Seyfert types, but this is at least partially due to the large contribution of the nuclear source in the Sy1's and intermediate Seyfert types.

V. M. M. M.'s research is funded by the Spanish Research Council (CSIC) under the I3P grant program. This work was supported in part by the Spanish Ministerio de Educación y Ciencia under grant AYA 2004-02703.

APPENDIX A

ATLAS OF THE SAMPLE

Brief description and notes on individual objects are given here. The descriptions refer to the F330W images unless it is said otherwise.

A1. Sy1, Sy1.2, AND Sy1.5 GALAXIES

Mrk 6 (Figs. 7.1, 9.1, 20.1): This object is a Sy1.5 galaxy with a very bright saturated core and some surrounding extended emission.

Mrk 40 (Figs. 7.2, 9.2, 20.2): This galaxy shows just a plain pointlike bright source.

Mrk 42 (Figs. 7.3, 9.3, 20.3): This is a very bright compact nucleus with a very tight wound spiral of star formation of $\sim$300 pc of radius. Many stellar clusters are individually resolved.

Mrk 231 (Figs. 7.4, 9.4, 20.4): This is a very powerful galaxy with a bright nucleus and some diffuse circumnuclear emission. There is an arc of star formation about 2 kpc to the south. This object falls next to the limit of its classification as a quasar and is also an *IRAS* galaxy, very luminous in the FIR (e.g., Soifer et al. 1987). It also shows a powerful megamaser emission, first detected by Baan (1985).

Mrk 493 (Figs. 7.5, 9.5, 20.5): Its morphology resembles that of Mrk 42, with a very bright nucleus and a tight wound spiral of star formation. However, the distance to this object is 50% higher than the distance to Mrk 42, so the individual stellar clusters are poorly resolved.

Mrk 915 (Figs. 7.6, 9.6, 20.6): This galaxy is a prototypical Sy1, with a very bright nucleus surrounded by diffuse emission.

NGC 3227 (Figs. 7.7, 8.1, 9.7, 20.7): This Sy1.5 galaxy shows a bright saturated nucleus and an off-center bar of star-forming regions, which is misaligned with the main galactic bar. This feature is probably caused by a close interaction with the dwarf elliptical NGC 3226. There is a star-forming region 100 pc to the north that is also visible in [O III] images (Schmitt & Kinney 1996). X-ray variability from its nuclear source has also been reported (Gondoin 2004).

NGC 3516 (Figs. 7.8, 9.8, 20.8): There is diffuse light surrounding the bright nucleus of this galaxy up to several hundred parsecs away. There is also evidence of obscuration by dust to the south and to the north of the nucleus. The northern dusty patches trace a spiral pattern.

NGC 4253 (Figs. 7.9, 9.9, 20.9): This is a barred spiral with several bright star-forming knots and star clusters. An important part of the star formation seems to be associated with the east part of the bar. The bar itself is visible in the UV image.

NGC 4593 (Figs. 7.10, 9.10, 20.10): Apart from the bright nucleus, there is a spiral structure of 1 kpc width with many individually resolved star clusters.

NGC 5548 (Figs. 7.11, 9.11, 20.11): This is a face-on spiral with a very bright nucleus. Several hundred parsecs to the north of the nucleus there is an arc of star formation, plus several scattered and relatively isolated stellar clusters still farther away.

NGC 5940 (Figs. 7.12, 9.12, 20.12): This is a face-on barred spiral with many star clusters and star-forming regions tracing the bar and spiral arms. Due to the combination of size and distance, most of this structure is included in the ACS HRC field of view.

NGC 6814 (Figs. 7.13, 9.13, 20.13): In this image there is not much visible apart from the plain PSF of the nucleus and some faint structure of the outer face-on spiral.

NGC 7469 (Figs. 7.14, 9.14, 20.14): This is very interesting object, with a faint spiral that becomes a conspicuous ring of star formation in the inner few hundred parsecs. Many stellar clusters are individually resolved within this region.

A2. Sy1.8 AND Sy1.9 GALAXIES

Mrk 334 (Figs. 7.15, 9.15, 20.15): This is a peculiar H II galaxy with irregular nuclear structure and strong star formation. It is also a strong IR source.

Mrk 471 (Figs. 7.16, 9.16, 20.16): This is very obscured by dust. The UV image shows only a pointlike nucleus and many scattered star-forming blobs and star clusters. In the optical image the barred spiral structure is better distinguished, with many dust lanes tracing the bar.

Mrk 516 (Figs. 7.17, 8.2, 9.17, 20.17): This galaxy is classified as an Sc. Although it looks quite regular in the IR, in the *U* band it is clearly asymmetric, with a star-forming arm to the south that has no counterpart to the north. The nucleus, which looks double in the WFPC2 image, is at the limit of the resolution and clearly separated from a bright blob right next to it to the north ($\sim$100 pc).

NGC 2639 (Figs. 7.18, 9.18, 20.18): The nucleus is heavily obscured, and no compact source is seen in the images. However, the main spiral structure is visible, with many stellar clusters in the outer region (several kiloparsecs away from the center).

NGC 3031 (M81; Figs. 7.19, 9.19, 20.19): This is the largest galaxy of one of the nearest groups. It is a typical Sa type, with a big bulge that fills the whole field of view of the camera. Some dust lanes are seen in the inner region, although no young star clusters are clearly visible in the UV image. Ho et al. (1995) describe it as a LINER.

NGC 3786 (Figs. 7.20, 9.20, 20.20): This galaxy shows a nuclear ring of a few hundred parsec radius in *HST* optical images that is incomplete in the UV. An ionization cone coming from the compact nucleus, to the southeast, is clearly detected.

NGC 4258 (M106; Figs. 7.21, 9.21, 20.21): The compact nucleus is resolved in our observation. There are many stellar clusters that can be studied individually, and there is a vast amount of absorption by dust in the southwest half of the image. This galaxy hosts a water-masing disk that led to the second-best determination of the mass of a supermassive black hole (SMBH) after the one in the Milky Way (Miyoshi et al. 1995).

NGC 4395 (Figs. 7.22, 9.22, 20.22): This is one of those objects for which the nucleus is at the limit of resolution. It is the object of the latest Hubble type in our sample (Sm). With such a small contribution of the bulge, only several scattered stellar clusters are seen apart from the nucleus and a region of diffuse light 10–20 pc to the west of it.

NGC 4565 (Figs. 7.23, 9.23, 20.23): This is a nearby edge-on galaxy. The nuclear region is thus very obscured at this wavelength, with conspicuous dust absorption. The nucleus appears partially resolved.

NGC 5033 (Figs. 7.24, 9.24, 20.24): This galaxy shows an unresolved nucleus together with an ionization cone open to the east (see Mediavilla et al. 2005). Heavy absorption to the west may be responsible for this asymmetry. There is an interesting feature consisting of a bright bar of light coming from the nucleus and extending 2″ to the north. This might be scattered light from the AGN or part of the extended narrow-line region.

NGC 5273 (Figs. 7.25, 9.25, 20.25): This is a lenticular galaxy with the typical morphology of an early-type galaxy. It shows a pointlike nucleus with extended light emission within the central 100 pc. There are some bright areas and dark lanes. The morphology seen with F606W is very similar, suggesting that the dark lanes are caused by thick dust clouds.

NGC 5674 (Figs. 7.26, 8.3, 9.26, 20.26): Although classified as a barred spiral in the RC3 catalog, this galaxy clearly shows a ring in UV light. The nuclear morphology is very interesting, with several clumps and stellar clusters embedded in diffuse emission in the central few hundred parsecs.

UGC 1395 (Figs. 7.27, 9.27, 20.27): This object shows a partially resolved nucleus and a circular shell of $\sim$200 pc radius.

UGC 12138 (Figs. 7.28, 9.28, 20.28): This shows a bright pointlike nucleus and diffuse emission adjacent to the north. To larger scales (several kiloparsecs) it shows a faint filamentary structure.

A3. Sy2 GALAXIES

CGCG 164−019 (Figs. 7.29, 9.29, 20.29): This Sy2 galaxy shows a bright nucleus and a wide-open spiral pattern. Some star clusters and knots are visible within the inner kiloparsec region, as well as diffuse light that might come from an unresolved stellar component.

Circinus (Figs. 7.30, 9.30, 20.30): This is a nearby spiral with a heavily obscured nucleus. The most prominent feature is a central ring of diffuse light and a star-forming blob 200 pc to the south. The Galactic latitude of this object is very low, so the image may suffer from foreground-star contamination. This galaxy is known to host a nuclear water-masing disk on a subparsec scale (Greenhill et al. 2003) and to have a kiloparsec-scale ionization cone (Marconi et al. 1994).

ESO 103-G35 (Figs. 7.31, 9.31, 20.31): No compact nuclear source is seen in the UV image, but only diffuse light and some blobs. The nuclear region is crossed by dust lanes, which gives it its chaotic structure.

ESO 137-G34 (Figs. 7.32, 9.32, 20.32): Neither the UV nor the optical image show an evident nucleus for this object. It has a patchy and chaotic structure with abundant dust lanes and some bright blobs. It is by far the object in the sample most contaminated by foreground stars, which is evident from the WFPC2 image. With a plate scale of 5 pc pixel^{-1}, it is difficult to distinguish a star cluster from a foreground star.

ESO 138-G1 (Figs. 7.33, 9.33, 20.33): This has a compact nucleus close to our limit of resolution and a bright asymmetric circumnuclear zone of diffuse light. The east part looks like an ionization cone or scattered light from the AGN.

ESO 362-G8 (Figs. 7.34, 9.34, 20.34): This object shows extended light emission around its resolved nucleus, with dusty patches. No stellar clusters or blobs are seen in the circumnuclear region.

Fairall 49 (IR 1832−594; Figs. 7.35, 9.35, 20.35): Within the central kiloparsec, this object shows a wound spiral that ends up in an asymmetric ring of star-forming knots. Several separated star clusters are seen, as well as a bright resolved nucleus. Malkan et al. (1998) found a nonresolved nuclear source in the IR. We can

resolve the nucleus in our UV image. Maiolino & Rieke (1995) have reclassified it as a Sy1.8 galaxy, although we have considered here the traditional classification as an Sy2.

IC 2560 (Figs. 7.36, 9.36, 20.36): A dust spiral is better seen in the optical images. In the UV an irregular extended emission surrounds the resolved nucleus.

IC 4870 (Figs. 7.37, 9.37, 20.37): Some extended filaments, as well as a lot of faint star clusters, are seen in this nucleus. There are also some bright clusters and a very bright pointlike source in the center. This object may in fact be an extragalactic H II region with unusually high ionization lines (Malkan et al. 1998), and the pointlike source might actually be a field star.

IC 5063 (Figs. 7.38, 9.38, 20.38): This shows very bright, compact, but resolved blobs within the nuclear region and some bright filaments along the southeast-northwest direction. Those could be scattered light from the AGN.

Mrk 461 (Figs. 7.39, 9.39, 20.39): This galaxy shows a resolved nucleus and a faint spiral structure some kiloparsecs wide.

Mrk 477 (Figs. 7.40, 9.40, 20.40): This compact galaxy hosts a very luminous Sy2 nucleus that has been proved by spectropolarimetry to have a hidden Sy1 (Tran et al. 1992). Heckman et al. (1997) have shown that it hosts a very compact nuclear starburst. The galaxy is interacting with a companion 50″ to the north. The nucleus is extended, and it shows a bright blob close to the northeast. There is, as well, an arc of star formation farther in the same direction.

Mrk 1210 (Figs. 7.41, 8.4, 9.41, 20.41): This is a compact face-on spiral. The tight wound spiral structure is visible in our image more like a ring, as traced by star-forming regions. The bright nucleus appears double at close inspection. Tran et al. (1992) showed, by spectropolarimetry, the presence of a hidden BLR.

NGC 449 (Figs. 7.42, 8.5, 9.42, 20.42): This object shows a bright resolved nucleus and several stellar clusters and knots. Star-forming regions and dust lanes trace a highly inclined spiral.

NGC 1144 (Figs. 7.43, 9.43, 20.43): This belongs to an interacting pair of galaxies (NGC 1143-1144). It shows a very distorted spiral structure with a circumnuclear ring traced out by dust lanes and bright regions. The nucleus is crossed by dark patches of dust.

NGC 1320 (Figs. 7.44, 9.44, 20.44): Although resolved, it possesses a bright compact nucleus. Most of the light is confined to a region of less than 100 pc wide. There is also a remarkable bright and narrow filament extending to the northwest. Dust lanes and extended emission trace a tight spiral pattern, although no stellar clusters are clearly detected in our image.

NGC 1672 (Figs. 7.45, 9.45, 20.45): This barred spiral harbors a very intense starburst within the inner kiloparsec. Many bright stellar clusters are individually resolved in the near-UV image. The star formation is mostly arranged in a ring, inside which there is also extended diffuse emission. The dust distribution seems completely asymmetrical, with heavy absorption to the northeast half of the nuclear region.

NGC 3081 (Figs. 7.46, 8.6, 9.46, 20.46): This is a peculiar ringed galaxy, with two nested rings, the smaller of which is shown in our F330W image. It has a bright resolved compact nucleus, with a bright ionization cone extending to the north. There is, as well, an important star-forming region ~300 pc to the southeast of the nucleus.

NGC 3362 (Figs. 7.47, 9.47, 20.47): Many stellar clusters and star-forming regions trace out a wide-open spiral pattern. The nucleus is resolved and elongated, and has an extension to the west in the form of a bright filament.

NGC 3393 (Figs. 7.48, 9.48, 20.48): Kondratko et al. (2006) have recently detected signatures of a water-masing disk on the subparsec scale, around the central SMBH. The image shows an S-shaped, bright, symmetric filament, which seems to be an ionization cone from the central engine.

NGC 3486 (Figs. 7.49, 9.49, 20.49): This is a borderline object between a Seyfert and a LINER galaxy, classified as Sy2 by Ho et al. (1997). It has a bright nucleus and extended emission with dust patches spiraling inward.

NGC 3982 (Figs. 7.50, 9.50, 20.50): Although this galaxy was classified as ringed in the RC3 catalog, in our *Hubble* images this feature is clearly identified as a spiral of star-forming regions, star clusters, and dust lanes.

NGC 4303 (M61; Figs. 7.51, 9.51, 20.51): This has been reclassified as a low-luminosity AGN, although in the original proposal it was included as an Sy2. The nucleus is known to host a compact star cluster as the main source of ionizing radiation (Colina et al. 2002). This nucleus is unresolved in our F330W image. It posses a conspicuous star-forming ring at ~250 pc radius, with many clusters individually resolved.

NGC 4725 (Figs. 7.52, 9.52, 20.52): The nuclear morphology of this early-type spiral shows not many features apart from the bright, resolved nucleus surrounded by extended emission with a clear exponential profile.

NGC 4939 (Figs. 7.53, 9.53, 20.53): The most noticeable feature of this nucleus is a biconical ionization structure coming out from the central source.

NGC 4941 (Figs. 7.54, 9.54, 20.54): This shows extended emission crossed by dark dust lanes. The nucleus has a compact clumpy structure with a bright compact core.

NGC 5005 (Figs. 7.55, 9.55, 20.55): The nucleus has both clumpy and diffuse emission, with a very broad dust lane obscuring the north part of the image. A spiral arm is visible to the south, with several isolated star clusters and richer star-forming regions.

NGC 5135 (Figs. 7.56, 8.7, 9.56, 20.56): This is a nice example of a very strong nuclear starburst, with many bright star clusters individually resolved and two wide-open spiral arms, traced by star-forming regions.

NGC 5194 (M51; Figs. 7.57, 8.8, 9.57, 20.57): The nucleus is completely obscured and surrounded by bright extended emission and crossed by dark dust lanes. The inner several hundred parsecs show some few isolated star clusters, while the outer regions are richly crowded with clusters and star-forming regions.

NGC 5256 (Figs. 7.58, 9.58, 20.58): This object is in fact a merging system with a double nucleus separated by ~5 pc. We have studied the northeastern nucleus, which is outstandingly brighter in our near-UV image than its southwestern companion. Actually, this nucleus has been classified as a LINER in the literature (Osterbrock & Dahari 1983). The structure of the nucleus is compact, clumpy, and irregular.

NGC 5283 (Figs. 7.59, 9.59, 20.59): The nucleus is bright and clumpy, with several almost adjacent objects. It shows filamentary structure of gas extending from the nucleus to the northeast.

NGC 5347 (Figs. 7.60, 9.60, 20.60): This is a ringed and barred spiral, although in our image only the inner 100 pc are distinguishable. The nucleus is very bright, and there is a conical opening to the northeast. There is also extended and quite homogeneous emission more obvious to the north side of the nucleus.

NGC 5695 (Figs. 7.61, 9.61, 20.61): The nucleus is compact but resolved, with a blob 0.2″ to the north. There is faint diffuse emission around it that follows a de Vaucouleurs profile.

NGC 5728 (Figs. 7.62, 9.62, 20.62): This is a peculiar galaxy with a neatly distorted ring of star-forming regions. The nucleus is completely obscured, and it shows an obvious ionization cone opening to the east.

NGC 6300 (Figs. 7.63, 9.63, 20.63): This galaxy is heavily obscured, so only faint diffuse emission can be appreciated in our image.

NGC 6951 (Figs. 7.64, 9.64, 20.64): This object shows a very regular ring of star-forming regions and stellar clusters. Inside the ring the surface brightness remains constant. The nucleus is diffuse and extended, with a couple of brighter blobs.

NGC 7130 (Figs. 7.65, 8.9, 9.65, 20.65): This shows an interesting morphology, with a ring and an inner bar. It is very rich in star-forming knots and stellar clusters, with a very bright region that is off-center from the ring. We have chosen as the galaxy center the centroid of the brightest of these blobs. The morphology of the center in F330W coincides with that of F210M presented in González Delgado et al. (1998).

NGC 7212 (Figs. 7.66, 9.66, 20.66): This galaxy belongs to a compact group of interacting galaxies. Spectropolarimetric studies have shown the presence of a hidden BLR (Tran et al. 1992). It shows a clumpy nuclear morphology and irregular diffuse emission.

NGC 7319 (Figs. 7.67, 9.67, 20.67): This object has the lowest measured UV flux in the sample. The nucleus is faint and shows an ionization cone opening to the north.

NGC 7479 (Figs. 7.68, 9.68, 20.68): The nucleus is small and resolved, and there are some scattered star clusters throughout the field of view. There is a remarkable chain of bright clusters 5″ to the south of the nucleus that has a north-south alignment.

NGC 7496 (Figs. 7.69, 9.69, 20.69): This barred spiral hosts a very powerful starburst in its center. In the image many star clusters can be seen embedded in diffuse emission. The center has been chosen as the brightest object in the field.

NGC 7674 (Figs. 7.70, 8.10, 9.70, 20.70): This is an obvious spiral structure with many star-forming regions. The nucleus is very bright and embedded in extended diffuse emission and surrounded by an arc of star formation.

NGC 7743 (Figs. 7.71, 9.71, 20.71): This galaxy is classified as an SB, although in our near-UV image no signs of the spiral structure can be detected. The nucleus is bright and surrounded by diffuse emission that appears brighter to the south.

UGC 1214 (Figs. 7.72, 8.11, 9.72, 20.72): The nucleus is very bright and is surrounded by a kiloparsec-scale symmetrical structure that seems to be an ionization cone.

UGC 2456 (Figs. 7.73, 8.12, 9.73, 20.73): This has a bright clumpy nucleus and S-shaped extended emission with three bright stellar clusters in it.

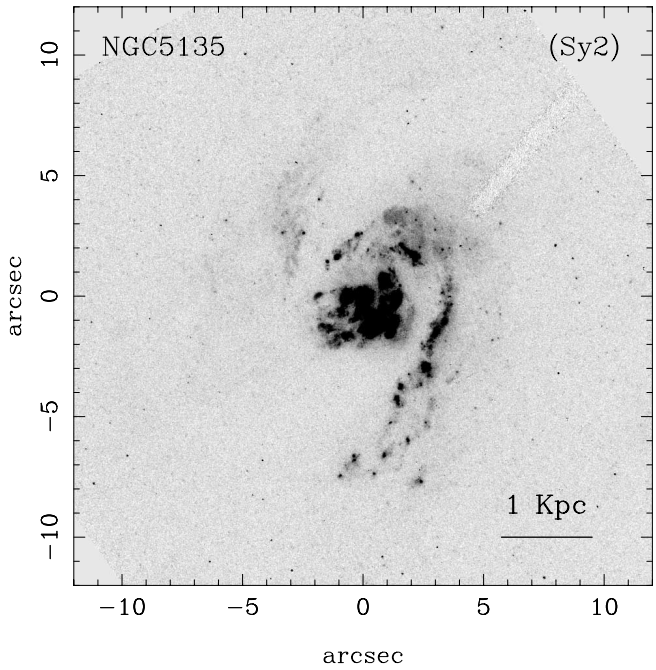

FIG. 20.56. Field-of-View Image of NGC 5135.

FIG. SET 20.—ACS images showing the fields of view. North is up, and east to the left. [*See the electronic edition of the Journal for* Figs. 20.1–20.75.]

UGC 6100 (Figs. 7.74, 9.74, 20.74): Although the S/N in the image is low, a spiral pattern with several star-forming regions is detected. The nucleus is extended and diffuse.

UM 625 (Figs. 7.75, 9.75, 20.75): This galaxy has a very bright compact nucleus that is partially resolved in our image. It also possesses a bright star cluster ∼150 pc directly to the west. Apart from this, the emission is diffuse and compact, as most of the light is enclosed within 1″ from the nucleus.

A4. VISUAL CATALOG

An image atlas of all the objects is presented. We show the whole field of view of the near-UV images in Figure Set 20. In most cases these figures show additional and complementary information to that of Figure Sets 7 and 8.

REFERENCES

Alonso-Herrero, A., Quillen, A. C., Rieke, G. H., Ivanov, V. D., & Efstathiou, A. 2003, AJ, 126, 81
Antonucci, R. 1993, ARA&A, 31, 473
Antonucci, R. R. J., & Miller, J. S. 1985, ApJ, 297, 621
Baan, W. A. 1985, Nature, 315, 26
Bershady, M. A., Jangren, A., & Conselice, C. J. 2000, AJ, 119, 2645
Böker, T., Laine, S., van der Marel, R. P., Sarzi, M., Rix, H.-W., Ho, L. C., & Shields, J. C. 2002, AJ, 123, 1389
Cardelli, J. A., Clayton, G. C., & Mathis, J. S. 1989, ApJ, 345, 245
Carollo, C. M., Stiavelli, M., Seigar, M., de Zeeuw, P. T., & Dejonghe, H. 2002, AJ, 123, 159
Cid Fernandes, R., Gu, Q., Melnick, J., Terlevich, E., Terlevich, R., Kunth, D., Rodrigues Lacerda, R., & Joguet, B. 2004, MNRAS, 355, 273
Cid Fernandes, R., Heckman, T., Schmitt, H., Delgado, R. M. G., & Storchi-Bergmann, T. 2001, ApJ, 558, 81
Cid Fernandes, R. J., & Terlevich, R. 1995, MNRAS, 272, 423
Colina, L., García Vargas, M. L., Mas-Hesse, J. M., Alberdi, A., & Krabbe, A. 1997, ApJ, 484, L41
Colina, L., González Delgado, R., Mas-Hesse, J. M., & Leitherer, C. 2002, ApJ, 579, 545
Conselice, C. J. 1997, PASP, 109, 1251
Cruz-González, I., Carrasco, L., Serrano, A., Guichard, J., Dultzin-Hacyan, D., & Bisiacchi, G. F. 1994, ApJS, 94, 47
Dahari, O., & de Robertis, M. M. 1988, ApJS, 67, 249
de Grijp, M. H. K., Keel, W. C., Miley, G. K., Goudfrooij, P., & Lub, J. 1992, A&AS, 96, 389
Falcke, H., Wilson, A. S., & Simpson, C. 1998, ApJ, 502, 199
Ferrarese, L., & Merritt, D. 2000, ApJ, 539, L9
Ferrarese, L., et al. 2006, ApJ, 644, L21
Ferruit, P., Wilson, A. S., & Mulchaey, J. S. 2000, ApJS, 128, 139
Freedman, W. L., et al. 1994, ApJ, 427, 628
Freeman, K. C. 1970, ApJ, 160, 811
Freeman, K. C., et al. 1977, A&A, 55, 445
Gebhardt, K., et al. 2000, ApJ, 539, L13
Gondoin, P. 2004, Nucl. Phys. B Proc. Suppl., 132, 181
González Delgado, R. M., Heckman, T., & Leitherer, C. 2001, ApJ, 546, 845
González Delgado, R. M., Heckman, T., Leitherer, C., Meurer, G., Krolik, J., Wilson, A. S., Kinney, A., & Koratkar, A. 1998, ApJ, 505, 174
Greenhill, L. J., et al. 2003, ApJ, 590, 162
Gu, Q., Melnick, J., Cid Fernandes, R., Kunth, D., Terlevich, E., & Terlevich, R. 2006, MNRAS, 366, 480

Heckman, T. M., González-Delgado, R., Leitherer, C., Meurer, G. R., Krolik, J., Wilson, A. S., Koratkar, A., & Kinney, A. 1997, ApJ, 482, 114
Ho, L. C., Filippenko, A. V., & Sargent, W. L. 1995, ApJS, 98, 477
———. 1997, ApJS, 112, 315
Huchra, J., & Burg, R. 1992, ApJ, 393, 90
Kinney, A. L., Bohlin, R. C., Calzetti, D., Panagia, N., & Wyse, R. F. G. 1993, ApJS, 86, 5
Kondratko, P. T., et al. 2006, ApJ, 638, 100
Lauer, T. R., et al. 1995, AJ, 110, 2622
Lipovetsky, V. A., Neizvestny, S. I., & Neizvestnaya, O. M. 1988, Soobshcheniya Spetsial'noj Astrofiz. Obs., 55, 5
Magorrian, J., et al. 1998, AJ, 115, 2285
Maiolino, R., & Rieke, G. H. 1995, ApJ, 454, 95
Malkan, M. A., Gorjian, V., & Tam, R. 1998, ApJS, 117, 25
Marconi, A., Moorwood, A. F. M., Origlia, L., & Oliva, E. 1994, Messenger, 78, 20
McLeod, K. K., & Rieke, G. H. 1995, ApJ, 441, 96
Mediavilla, E., Guijarro, A., Castillo-Morales, A., Jiménez-Vicente, J., Florido, E., Arribas, S., García-Lorenzo, B., & Battaner, E. 2005, A&A, 433, 79
Meurer, G. R., Heckman, T. M., Leitherer, C., Kinney, A., Robert, C., & Garnett, D. R. 1995, AJ, 110, 2665
Miller, J. S., & Goodrich, R. W. 1990, ApJ, 355, 456
Miyoshi, M., Moran, J., Herrnstein, J., Greenhill, L., Nakai, N., Diamond, P., & Inoue, M. 1995, Nature, 373, 127
Moles, M., Márquez, I., & Pérez, E. 1995, ApJ, 438, 604
Morris, S. L., & Ward, M. J. 1988, MNRAS, 230, 639
Mulchaey, J. S., Wilson, A. S., & Tsvetanov, Z. 1996, ApJS, 102, 309
Nelson, C. H., MacKenty, J. W., Simkin, S. M., & Griffiths, R. E. 1996, ApJ, 466, 713
Oliva, E., Salvati, M., Moorwood, A. F. M., & Marconi, A. 1994, A&A, 288, 457
Osterbrock, D. E. 1981, ApJ, 249, 462
Osterbrock, D. E., & Dahari, O. 1983, ApJ, 273, 478
Pavlovsky, C., et al. 2004, ACS Data Handbook, Ver. 3.0 (Baltimore: STScI)
Pérez, E., González-Delgado, R., Tadhunter, C., & Tsvetanov, Z. 1989, MNRAS, 241, 31P
Quillen, A. C., McDonald, C., Alonso-Herrero, A., Lee, A., Shaked, S., Rieke, M. J., & Rieke, G. H. 2001, ApJ, 547, 129
Rossa, J., van der Marel, R. P., Böker, T., Gerssen, J., Ho, L. C., Rix, H.-W., Shields, J. C., & Walcher, C.-J. 2006, AJ, 132, 1074
Sanders, D. B., & Mirabel, I. F. 1996, ARA&A, 34, 749
Schmitt, H. R., Donley, J. L., Antonucci, R. R. J., Hutchings, J. B., & Kinney, A. L. 2003, ApJS, 148, 327
Schmitt, H. R., & Kinney, A. L. 1996, ApJ, 463, 498
Sirianni, M., et al. 2005, PASP, 117, 1049
Soifer, B. T., Neugebauer, G., & Houck, J. R. 1987, ARA&A, 25, 187
Storchi-Bergmann, T., Bica, E., & Pastoriza, M. G. 1990, MNRAS, 245, 749
Storchi-Bergmann, T., Kinney, A. L., & Challis, P. 1995, ApJS, 98, 103
Storchi-Bergmann, T., & Pastoriza, M. G. 1989, ApJ, 347, 195
Storchi-Bergmann, T., Raimann, D., Bica, E. L. D., & Fraquelli, H. A. 2000, ApJ, 544, 747
Tadhunter, C., & Tsvetanov, Z. 1989, Nature, 341, 422
Terlevich, E., Díaz, A. I., & Terlevich, R. 1990, Rev. Mex. AA, 21, 218
Terlevich, R., Melnick, J., Masegosa, J., Moles, M., & Copetti, M. V. F. 1991, A&AS, 91, 285
Tran, H. D. 1995, ApJ, 440, 597
Tran, H. D., Miller, J. S., & Kay, L. E. 1992, ApJ, 397, 452
Tully, R. B. 1988, Nearby Galaxies Catalogue (Cambridge: Cambridge Univ. Press)
Walcher, C. J., Böker, T., Charlot, S., Ho, L. C., Rix, H.-W., Rossa, J., Shields, J. C., & van der Marel, R. P. 2006, ApJ, 649, 692
Whittle, M. 1992, ApJS, 79, 49
Wilson, A. S., Ward, M. J., & Haniff, C. A. 1988, ApJ, 334, 121
Wilson, C. D., Harris, W. E., Longden, R., & Scoville, N. Z. 2006, ApJ, 641, 763